Article

Self-Consistent Crystal Plasticity Modeling of Slip-Twin Interactions in Mg Alloys

Mukti Patel [1,2], YubRaj Paudel [1,*], Shiraz Mujahid [1] (ID), Hongjoo Rhee [1,2] and Haitham El Kadiri [1,2,3,*]

1 Center for Advanced Vehicular Systems, Mississippi State University, Mississippi State, MS 39762, USA
2 Department of Mechanical Engineering, Mississippi State University, Mississippi State, MS 39762, USA
3 School of Automotive Engineering, Université Internationale de Rabat, Rabat-Shore Rocade Rabat-Salé, Rabat 11103, Morocco
* Correspondence: yubraj@cavs.msstate.edu (Y.P.); elkadiri@me.msstate.edu (H.E.K.)

Abstract: Parsing the effect of slip-twin interactions on the strain rate and thermal sensitivities of Magnesium (Mg) alloys has been a challenging endeavor for scientists preoccupied with the mechanical behavior of hexagonal close-packed alloys, especially those with great latent economic potential such as Mg. One of the main barriers is the travail entailed in fitting the various stress–strain behaviors at different temperatures, strain rates, loading directions applied to different starting textures. Taking on this task for two different Mg alloys presenting different textures and as such various levels of slip-twin interactions were modeled using visco-plastic self-consistent (VPSC) code. A recently developed routine that captures dislocation transmutation by twinning interfaces on strain hardening within the twin lamellae was employed. While the strong texture was exemplified by traditional rolled AZ31 Mg alloys, the weak texture was represented by ZEK100 Mg alloy sheets. The transmutation model incorporated within a dislocation density based hardening model showed enhanced flexibility in predicting the complex strain rate and thermal sensitive behavior of Mg textures' response to various mechanical loading schemes.

Keywords: self-consistent model; VPSC; magnesium; ZEK100; AZ31

1. Introduction

Magnesium had been of particular interest because of its lightweight and high specific strength capability, making it favorable for applications in the automobile and aeronautical industry. Further, the metal's advantage in strength to weight ratio over other conventional metals like steel and aluminum along with the drive to reduce fuel consumption and emissions has stirred scientists to focus their attention towards engineering magnesium. Magnesium alloys have also found their applications in the biomedical field as they are biocompatible. A major obstacle to magnesium's use is its low room temperature ductility due to its hexagonal close-packed (HCP) structure which affects the metal's room temperature formability and crash-worthiness. One of the most widely used magnesium alloys for commercial application, AZ31, has demonstrated high plastic deformation which can lead to fracture during the forming process [1]. Magnesium's use in the structural components of automobiles [2] requires processing by stamping it into thin sheets to fit the component's shape, making room temperature formability an important property to optimize. Predicting the onset of fracture with the help of a forming limit diagram can help develop suitable methods for forming the sheet. Magnesium also exhibits inferior energy absorption ability compared to Aluminum and Steel at room temperature, affecting its crashworthiness and making it undesirable for safety-critical components. We can identify the root cause for early hardening and damage at the atomistic level by studying the deformation mechanism exhibited by HCP materials.

Mechanical properties of magnesium are greatly affected by profound twinning at an early stage, as compared to ideally ductile face centered cubic (FCC) materials that demand

high critical resolved shear stress (CRSS) for the twin to propagate. The easy slip system for FCC lies on its pyramidal plane, allowing effortless deformation, with a high Schmid factor system available regardless of the loading direction. The same is not true for HCP materials as the easy slip system lies in the basal plane, requiring low CRSS to activate as compared to non-basal $\langle c + a \rangle$ slip systems thus, preventing $\langle c \rangle$-axis deformation. The asymmetry and anisotropy observed in magnesium are contingent on the loading directions, activating different deformation modes when loaded in through-thickness direction versus in-plane direction given the strongly organized texture [3,4].

It is known that a minimum of five independent deformation modes need to be active for hardening as well as damage to occur in polycrystalline materials encouraging uniform plasticity [5]. The slip modes identified for magnesium are basal $\langle a \rangle$, prismatic $\langle a \rangle$, and pyramidal $\langle c + a \rangle$. Basal $\langle a \rangle$ slip can be activated very easily while prismatic $\langle a \rangle$ is slightly harder to activate in Mg when compared to basal slip. The Burger vectors within the (0001) basal plane are dislocation of $\frac{1}{3}\{11\bar{2}0\}$ type, of which only two are independent, thus not satisfying the criteria for five independent slip systems [6]. A pyramidal, $\langle c + a \rangle$ type of slip system is needed to include the component on the $\langle c \rangle$-axis.

At room temperature, the CRSS required to activate a pyramidal slip system is high enough to be preceded by $\{10\bar{1}2\}$ tension/extension twinning causing early damage. It is the predominant twinning mechanism in most of the HCP metals producing $\langle c \rangle$-axis extension when the c/a ratio is less than $\sqrt{3}$ and $\langle c \rangle$-axis compression when $\frac{c}{a}$ is greater [7]. The $\{10\bar{1}2\}\langle10\bar{1}1\rangle$ tension/ extension twin, and $\{10\bar{1}1\}\langle10\bar{1}2\rangle$ compression/contraction twin are two $\langle c \rangle$-axis deformation twins most commonly observed in Mg alloys. Tension twin is substantially easier to activate as compared to compression twin that requires higher shear stress. The presence of twinning leads to slip and twin interaction, rushing fracture due to strain incompatibility [8–10]. The CRSS for tension twin is as low as 2 MPa [11], causing it to propagate early during the deformation process and responsible for the mechanical anisotropy in magnesium. The $\{10\bar{1}2\}$ twin is observed when the crystal is strained parallel to $\langle c \rangle$-axis forming tension twin or compressed perpendicular to $\langle c \rangle$-axis forming extension twin [12]. The resulting stress–strain response depicts anisotropy between rolling direction (RD) (in-plane compression (IPC)) and normal direction (ND) (through-thickness compression (TTC)) magnesium sample loaded in tension or compression [13]. In RD compression, the texture is aligned to cause $\langle c \rangle$-axis extension by compressing perpendicular to $\langle c \rangle$-axis, activating basal slip systems along with profuse tension twinning that is hardly observed when compressing parallelly to $\langle c \rangle$-axis [14]. Twinning hardens the material as the parent matrix reorients prompting compressing along the $\langle c \rangle$-axis. This calls for significant pyramidal $\langle c + a \rangle$ slip resulting in the steep hardening curve, leading to an onset of $\{10\bar{1}1\}$ type twin, associated with causing damage to failure. $\{10\bar{1}1\}$ type twin requires very high CRSS to activate and accommodate strain by compression or contraction of $\langle c \rangle$-axis. Similar slip systems are observed for compression loading in the ND direction, where high yield stress and initial hardening result from pyramidal $\langle c + a \rangle$ necessary for $\langle c \rangle$-axis deformation. Shear banding associated with pyramidal $\langle c + a \rangle$ is observed initiating early damage and failure. Anisotropy analogous to compression is observed in tension. One would expect more ductility as prismatic $\langle a \rangle$ will dominate, $\{10\bar{1}1\}$ would not be active as it would require high CRSS, and shear banding will be absent. Contrary to expectation, twin nucleates early at a very low strain resulting in cracks. The early onset of contraction twinning is associated with hydrostatic pressure. Twinning is not just shear but is also accompanied by shuffle possessing diffusional nature [8,15] which is driven by hydrostatic pressure, encouraging the threshold stress. At the same orientation, magnesium has different saturation stress despite similar mechanisms being at play; thus, another mechanism must be at work here.

Various polycrystalline models have been developed over the years [16–21] to predict plastic behavior and texture evolution. It has been challenging to effectually capture the effects of twinning on hardening owing to the crystallographic reorientation of the twin at propagation and the slip-twin interaction as the twin fraction grows. The method

proposed by Tomé et al. in 1991 [16], using the Predominant Twin Reorientation (PTR) scheme, accounts for the grain reorientation during deformation while keeping the volume fraction constant. In this case, the predominant twin causing a certain threshold of the grain to reorient would result in the entire grain reorienting, providing misleading texture. The scheme was enhanced to the Volume Fraction Transfer (VFT) scheme [17] by splitting the grains into cells once the twin has substantially grown and accounted for the volume fraction transfer contributed by each twin system during the deformation. The drawback of the VFT scheme is that the track of the original grain is lost. The model suggested by Kalindindi [18], provides an alternate solution to this problem by keeping a track of the volume fraction in each grain and relying on the initial orientation of the lattice instead of updating the crystal orientation after every time step. Though, this model fails to account for secondary twinning. Hardening is a response, not only to the texture evolution but also to the slip-slip, twin-twin, and slip-twin interactions which are subjective of the loading conditions and the initial texture. The above mentioned frameworks fail to predict the plastic response in HCP materials when either slip or twinning is not the dominant mechanism [22]. Recently developed polycrystalline models have utilized different approaches [23–26] at addressing the issue of hardening induced by slip-slip and slip-twin interaction which is contrary to using a latent hardening coefficient. Some of these models and their developments are discussed below.

1.1. Visco-Plastic Self-Consistent (VPSC) Model

A self-consistent theory to deforming large polycrystals was first proposed by Molinari et al. [27] and later developed into a VPSC model to include anisotropic behavior by Lebensohn and Tomé [17]. In their work, Lebensohn and Tomé used experimental data from Zirconium alloy to verify their model and predict texture evolution. In this section, we will discuss the equations implemented in the VPSC model. The resolved shear stress, plastic strain rate, and the shear rate induced by applied stress for a given slip system s takes the form

$$\tau_r^s = m_{ij}^s \sigma \tag{1}$$

$$\dot{\varepsilon} = m_{ij}^s \dot{\gamma}^s \tag{2}$$

$$\dot{\gamma}^s = \dot{\gamma}_0 \left(\frac{\tau_r^s}{\tau_c^s} \right)^n = \dot{\gamma}_0 \left(\frac{m_{ij}^s \sigma}{\tau_c^s} \right)^n \tag{3}$$

where, m_{ij}^s is a symmetric Schmid tensor, and σ is a stress tensor, $\dot{\gamma}_0$ is a reference rate, and n is inverse of strain rate sensitivity. Substituting Equation (3) in Equation (2) and summing over all the slip systems 's' in the grain we get the equation,

$$\dot{\varepsilon} = \dot{\gamma}_0 \sum_s \left(\frac{m^s : \sigma}{\tau_c^s} \right)^n = M_{ijkl}^{sec} \sigma_{kl} \tag{4}$$

The visco-plastic model makes an assumption of the grain being an inclusion that is embedded in a visco-plastic medium. The macroscopic strain rate is given by,

$$\bar{\dot{\varepsilon}}_{ij} = \bar{M}_{ijkl}^{sec} \bar{\sigma}_{kl} \tag{5}$$

The interaction equation between the macroscopic stress and strain rate and the stress and strain rate in the grain can be given by,

$$\left(M^{sec} : \sigma - \bar{M}^{sec} : \bar{\sigma} \right) = \left(\dot{\varepsilon} - \bar{\dot{\varepsilon}} \right) = -\widetilde{M} : \left(\sigma - \bar{\sigma} \right) \tag{6}$$

$$\text{where } \widetilde{M} = n^{eff} (I - S)^{-1} S \bar{M}^{sec}$$

here, $\widetilde{M}$ is an interaction tensor, $\bar{M}^{sec}$ is the compliance tensor, S is the visco-plastic Eshelby tensor, and n is a matrix multiplier ranging from secant to tangent ($0 < n < 1$). We can derive the stress in the grain from Equations (4) and (6),

$$\sigma_{ij} = \left(M^{sec} + \widetilde{M} \right)^{-1}_{ijmn} \left(M^{sec} + \widetilde{M} \right)_{mnkl} \bar{\sigma}_{kl} \tag{7}$$

Since the overall average stress in the grain needs to be equal to the macroscopic stress, macroscopic secant compliance can be computed interactively with an initial guess,

$$\left\langle \left(M^{sec} + \widetilde{M} \right)^{-1}_{ijmn} \left(M^{sec} + \widetilde{M} \right)_{mnkl} \right\rangle = I_{ijkl} \tag{8}$$

The visco-plasticity model gave an inclusion formalism using Eshelby tensor to capture the anisotropy of the grain and predict the texture. This forms a basis for the VPSC model which is enhanced and presented in the models following.

1.2. Composite Grain (CG) Model

The model proposed by Proust et al. [19] put forward a composite grain model that accounts for both the original and the reoriented twin fraction and the interaction between them in form of a latent hardening term associated with twin shear as the deformation progresses. The CG model keeps a track of the shear in each twin system in each grain, and the one with the maximum volume fraction is identified as the predominant twin system (PTS) given by,

$$f^{PTS} = \Delta\gamma^{PTS}/S \tag{9}$$

where, $\Delta\gamma$ is shear contributed by the twin system and S is the characteristic twin shear [19]. The PTS splits the grain into parallel twin lamellae equidistantly apart, seen in Figure 1. The model introduces d^c as the distance between the center of two planes and f^{PTS}_{max} gives the maximum volume fraction of the twin that has transformed inside the grain. As the twin nucleates within the grain of size d^g, the twin of thickness d^{twin} can grow to a maximum of d^{twin}_{max} under deformation giving, $d^{twin}_{max} = f^{PTS}_{max} d^c$.
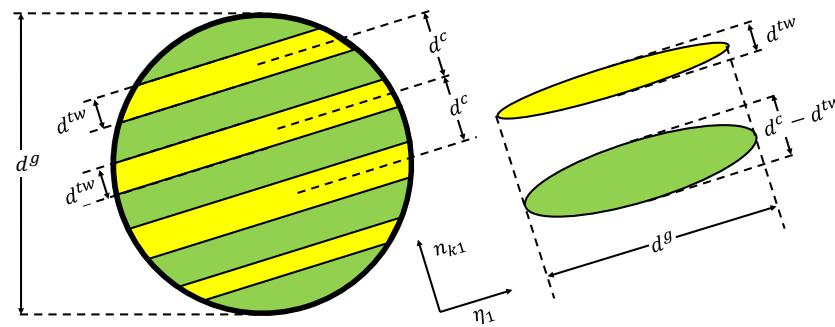

Figure 1. Representation of the orientation of the twins and the parent matrix with their distinctive dimensions employed in the formulation of the composite grain (CG) model [19].

Similarly, the fraction of the parent and the child twin evolved during the deformation is given by,

$$d^{twin} = f^{PTS} d^c$$
$$d^{matr} = \left(1 - f^{PTS}\right) d^c \tag{10}$$

Throughout the deformation process, the volume fraction of each twin system is tracked, and the system that exceeds the defined threshold volume fraction is determined to be PTS. Twin planes of the PTS will have a specific orientation relative to the twin and

slip of the other active systems. Introducing the mean free path for each system '*s*' for the twin and the matrix respectively,

$$d_{mfp}^{tw} = \frac{d^{twin}}{\sin \alpha}$$

$$d_{mfp}^{s} = \frac{d^{matr}}{\sin \alpha} \tag{11}$$

In the composite grain model, hardening of the slip in the matrix and twinning system in the twin can be expressed as a sum of the evolution of statistical dislocation with strain, the evolution of geometrically necessary dislocations (GND), and the Hall-Petch effect that arises from the presence of twin boundary as given in Equation (12). The statistical dislocation and GND terms are continuously updated as the grain deforms.

$$\tau^{s} = \tau_{STAT}^{s} + \tau_{GND}^{s} + \tau_{HP}^{s} \tag{12}$$

The τ_{STAT}^{s} term is the saturation Voce law associated with statistical dislocation plus a latent hardening coefficient $h^{ss'}$ coupling shear increment $\Delta \gamma^{s'}$ in system s' with the increase in strength in system s as given below where Γ is the accumulated shear in the grain.

$$\Delta \tau_{STAT}^{s} = \frac{d\hat{\tau}^{s}}{d\Gamma} \sum_{s'} h^{ss'} \Delta \gamma^{s'} \tag{13}$$

where,

$$\hat{\tau}_{(\Gamma)}^{S} = \tau_0 + \tau_1 \left\{ 1 - \exp \left(-\frac{\Gamma \theta_0}{\tau_1} \right) \right\} \tag{14}$$

The terms τ_0, $\tau_0 + \tau_1$, and θ_0 are the initial CRSS, the back-extrapolated CRSS, and the initial hardening rate, respectively. The correlation between the mean free path of the slip and twin with the PTS lamella is an idea central to the CG model. Karaman et al. [28] and Kok et al. [29] derived the dependency of the GND term on mean free path as given in Equation (15). The directional mean free path in Equations (15) and (16) are specific to each system, as previously shown in Equation (11).

$$\Delta \tau_{STAT}^{s} = \frac{h_m^s}{d_{mfp}^s \left(\tau_{STAT}^s + \tau_{GND}^s \right)} \Delta \gamma^s \tag{15}$$

The Hall-Petch term as given below,

$$\tau_{HP}^{s} = \frac{h_{HP}^s}{\sqrt{d_{mfp}^s}} \tag{16}$$

1.3. Dislocation Density-Based Model

The dislocation-density-based model was proposed by Beyerlein et al. [30] to take into account the limitation of temperature and strain rate effects on the deformation history based on dislocation density for slip. Previous models use parameters that could produce results only for a specific temperature and strain rate. The model uses dislocation density on each slip system governed by law, including a thermally activated recovery process that either annihilates or forms debris. The hardening law for slip addresses stages II–IV, and the hardening law for twin propagation accounts for temperature effects through interaction with slip dislocations. The hardening laws are implemented in the above-mentioned CG model [19] and implemented in the visco-plastic self-consistent (VPSC) polycrystalline model.

Hardening is based on updating critical resolved shear stress (CRSS) τ_c^s that depends on local microstructure encounter by the dislocation at each increment in the flow rule that calculates shear strain rate $\dot{\gamma}_s$ as shown in Equation (3). The slip resistance in the dislocation-density model includes effects from forest dislocation, dislocation debris, the Hall-Petch

effect on slip propagation based on dislocation mean free path. Here, s is the slip system that belongs to the slip mode α (e.g., basal, pyramidal, etc.).

$$\tau_c^s = \tau_0^\alpha + \tau_{forest}^\alpha + \tau_{deb}^\alpha + \tau_{HP}^\alpha \quad s \in \alpha \tag{17}$$

The slip resistance due to forest dislocation and debris terms are dictated by the given equations,

$$\tau_{forest}^\alpha = b^\alpha \chi \mu \sqrt{\rho^\alpha} \tag{18}$$

$$\tau_{deb}^\alpha = k_{deb} \mu b^\alpha \sqrt{\rho_{deb}} \log\left(\frac{1}{b^\alpha \sqrt{\rho_{deb}}}\right) \tag{19}$$

where, b is the Burgers vector, χ is a dislocation interaction factor less than 1 [31], and μ is the shear modulus. The Hall-Petch effect due to slip without twin propagation,

$$\tau_{HP}^s = \begin{cases} \mu HP^\alpha \sqrt{\dfrac{b^\alpha}{d_g}} & s \in \alpha \text{ without twins} \\ \mu HP^{\alpha\beta} \sqrt{\dfrac{b^\alpha}{d_{mfp}^{s,PTS}}} & s \in \alpha \text{ with twins present} \end{cases} \tag{20}$$

The evolution of dislocation-density using the thermal activation model proposed by Essmann et al. and Mecking et al. [32,33],

$$\frac{\partial \rho^\alpha}{\partial \gamma^\alpha} = \frac{\partial \rho_{generstion}}{\partial \gamma^\alpha} - \frac{\partial \rho_{removal}}{\partial \gamma^\alpha} = k_1^\alpha \sqrt{\rho^\alpha} - k_2^\alpha(\dot{\varepsilon}, T)\rho^\alpha \tag{21}$$

$$\frac{k_2^\alpha(\dot{\varepsilon}, T)}{k_1^\alpha} = \frac{\chi b^\alpha}{g^\alpha}\left(1 - \frac{kT}{D^\alpha(b^\alpha)^3}\ln\left(\frac{\dot{\varepsilon}}{\dot{\varepsilon}_0}\right)\right) \tag{22}$$

here, k_1^α is a rate-sensitivity parameter that accounts for dislocation generation, $k_2^\alpha(\dot{\varepsilon}, T)$ is a temperature and strain-rate dependent term that accounts for the lost dislocations. g^α is the activation energy, k is the Boltzmann constant, D^α is the drag stress, and (ε_0) is the reference strain rate, a function of material set to $10^7 \, s^{-1}$ for magnesium [34].

Resistance to twin propagation τ_c^t for a given twin system t, that belongs to the twin mode β, is the contribution from initial friction τ_0^β, the Hall-Petch effect, and the effect of slip.

$$\tau_c^t = \tau_0^\beta + \tau_{HP}^t + \tau_{slip}^\beta \quad t \in \beta \tag{23}$$

The Hall-Petch terms are given as follows,

$$\tau_{HP}^t \begin{cases} \dfrac{HP^\beta}{\sqrt{d_g}} & \text{without twins or when } t \in \beta \text{ and } t \text{ is PTS} \\ \dfrac{HP_{TW}^{\beta\beta'}}{\sqrt{d_{mfp}^s}} & \text{when } t \in \beta \text{ and } t \text{ is not PTS, PTS} \in \beta' \end{cases} \tag{24}$$

here, β represents different twin modes (e.g., $\{10\bar{1}2\}$ twinning) and β' represents the mode of PTS in the grain that can be the same as β.

The contribution to hardening due to the interaction between slip dislocations and twin systems is given by the following equation,

$$\tau_{slip}^\beta = \mu \sum_\alpha C^{\beta\alpha} b^\beta b^\alpha \rho^\alpha \tag{25}$$

In case that the slip hinders the propagation of the twin suppressing its growth, the term $C^{\beta\alpha}$ is positive. In the case where the slip dislocations have contributed to the propagation and growth of twin, $C^{\beta\alpha}$ is negative.

1.4. Dislocation Transmutation Scheme

In their work, El Kadiri and Oppedal [22] formulate governing equations that were incorporated in the dislocation density model of VPSC to include the hardening effects from dislocation transmutation. The authors have suggested that the hardening observed in the sigmoidal curve of HCP material due to profuse twinning is a result of dislocation transmutation and/or absorption by the twin boundary. Previous polycrystalline models have used Hall-Petch effects and high stacking fault slip modes with PTS to model the hardening.

As the twin boundary advances within the parent grain, the twin lamella consumes the dislocations already present in the parent matrix. The dislocations can either be completely absorbed by the twin interface producing disconnections or the dislocations change their Burgers vector and plane when assimilated into the twin lamella. The disconnection generated at the twin interface can aid twin propagation when colliding with other slips. The later mentioned dislocations mechanism is referred to as dislocation transmutation.

Transmutation transforms the matrix dislocations into sessile and glissile dislocations with a low local Schmid factor. These dislocations are immobile in nature and interact with the local dislocations within the twin, prompting very high latent hardening. This interaction is called the Basinski's mechanism [35] and is illustrated in Figure 2. Latent hardening induced due to transmutation mechanisms has not been adopted in previous crystal plasticity models, albeit the twin massively hardens compared to the matrix. The earlier models using the Hall-Petch effect based on latent hardening due to twin-slip interactions have been fair at reproducing the experimental stress–strain response, but they have failed at predict intermediate texture and/or twin volume fraction evolution [22].
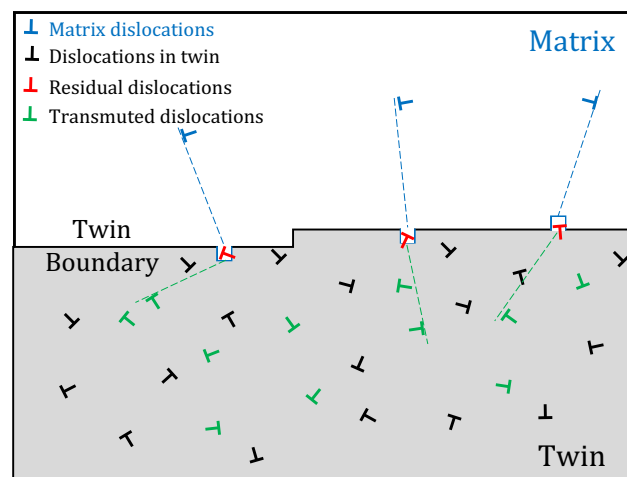

Figure 2. Illustration of the twin boundary propagating in the parent matrix instigating the dislocation transmutation mechanism and the subsequent latent hardening.

Oppedal et al. [13] have used numerical and experimental (pure Mg) means to demonstrate the influence of transmutation mechanism on the sharp hardening observed in Regime II due to profuse twinning. A modified version of the dislocation density model [30] was used in VPSC by incorporating the twin storage factor (TSF) to manipulate the hardening behavior. The latent hardening due to the Hall-Petch effect was turned off, and different TSF's were used to increase the dislocation density volume and harden the twin inside the matrix. Oppedal et al. were successfully able to reconstruct the hardening behavior for pure Mg in multiple compression loading paths signifying that mechanisms other than the Hall-Petch effects were at work. The excessive hardening in the twin compared to the parent matrix is not due to dislocation generation in the twin, but a result of the transmutation-induced latent hardening as dislocations multiplies within the twin [13]. In the case of through-thickness compression (TTC), where twinning is not dominant, the Hall-Petch effect has been able to provide satisfactory results but increasing

the dislocation density in the twin using TSF has been able to rationalize the different saturation stress between TTC and in-plane compression (IPC). The governing equation to update the dislocation density inside the twin volume fraction proposed by El Kadiri and Oppedal [22] is discussed below.

Consider a grain enclosing a twin lamella of volume fraction V^T undergoing deformation. At every small incremental deformation $d\varepsilon$, the twin expands uniformly on each side by a volume of $\frac{dV}{2}$. Dislocation density for a given dislocation type i in parent and the twin is given by ρ^{jP} and ρ^{iT} respectively. Consider a jth dislocation from a given deformation mode in parent grain, is transmuted to an ith dislocation upon twinning, then the increase in the density of the ith dislocation in the twin is calculated using the equation below

$$d\rho^{iTF}(V) = \frac{V^T \rho^{iT} + dV \sum_j \alpha_{ij} \rho^{jP}}{V^T + dV} \tag{26}$$

where, α_{ij} is a non-dimensional phenomenological second-order transmutation matrix measuring the fraction of j dislocations transmuted to i dislocations.

The present work aims to further validate transmutation in HCP, by recreating the mechanical behavior of a strongly textured and a weakly textured magnesium alloy at different loading conditions, temperatures, and strain rates. The VPSC polycrystalline framework [16,17] with temperature and strain rate independent dislocation density model [30] modified to include the dislocation transmutation scheme [22,36] is used in this work. The objective is to enhance the robustness of the crystal plasticity model through physics-based modification rather than purely empirical fitting methods.

2. Experimental Results and Discussion
2.1. Strongly Textured Magnesium AZ31

A 12 mm thick rolled, strongly basal textured sheet of AZ31 magnesium (3% Al, 1% Zn) was used to machine the samples for experiments. Tests were conducted in two different loading orientations, rolling direction (RD) or in-plane direction and normal direction (ND) or through-thickness direction to capture the anisotropy of AZ31. The test samples extracted in RD and ND were tested in both compression and tension at three different temperatures—293 K (20 °C), 373 K (100 °C), and 473 K (200 °C) under two different strain rates—0.001 s^{-1} and 0.1 s^{-1}. The test matrix is presented in Table 1 below. A total of twenty-four stress–strain responses were fit with the same set of hardening parameters.

Table 1. Matrix of tests used for fitting and testing crystal plasticity model. ($*$: Tests performed).

Magnesium AZ31							
Strain Rate (s^{-1})	Orientation	293 K		373 K		473 K	
		Tension	Compression	Tension	Compression	Tension	Compression
0.001	RD	$*$	$*$	$*$	$*$	$*$	$*$
	ND	$*$	$*$	$*$	$*$	$*$	$*$
0.1	RD	$*$	$*$	$*$	$*$	$*$	$*$
	ND	$*$	$*$	$*$	$*$	$*$	$*$
Magnesium ZEK100							
Strain Rate (s^{-1})	Orientation	293 K		373 K		473 K	
		Tension	Compression	Tension	Compression	Tension	Compression
0.001	RD	$*$	—	$*$	—	$*$	—
	30° to RD	$*$	—	$*$	—	$*$	—
	60° to RD	$*$	—	$*$	—	$*$	—
	TD	$*$	—	$*$	—	$*$	—

Compression and tension samples were extracted from the rolled sheet using water jet cutting for precision, considering three of the four samples were as small as 10 mm in size. The specimens used in this study are described below and presented in Figure 3:

1. Cylindrical specimens 10 mm in diameter and 10 mm in length were used for compression testing in ND and RD orientation.
2. A mini dog bone specimen, 2 mm in thickness was cut for tension testing in ND due to limitations in the available length in the ND direction of the rolled AZ31 sheet.
3. Round tensile dog bone specimen was designed for tension test in RD.
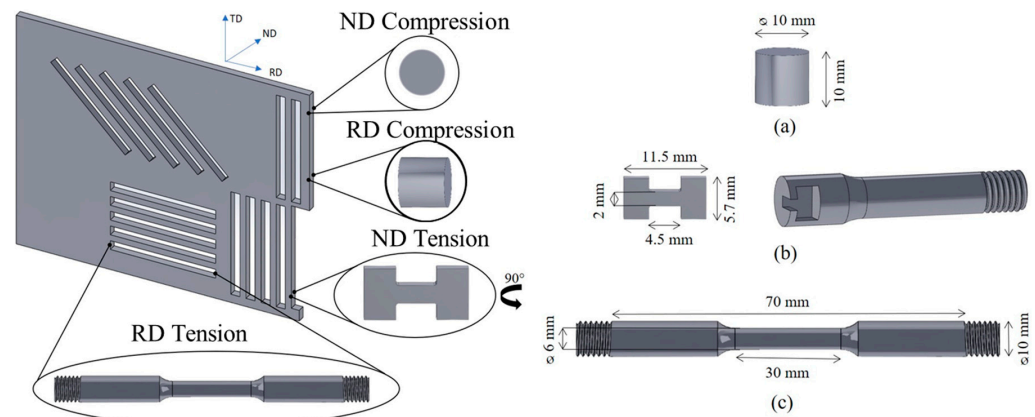

Figure 3. Illustration of orientations of test specimens extracted from rolled AZ31 magnesium alloy sheet. (**a**) Dimensions of the AZ31 magnesium compression test specimens extracted from ND and RD orientations. (**b**) Mini dog bone tension specimen cut in ND and the grip designed for the mini sample to conduct the test. (**c**); Round dog bone tension specimen in RD.

Initial texture for AZ31 investigated in this study, obtained via neutron diffraction by Los Alamos National Laboratory (LANL). The initial texture with 15,552 distinct grains was mapped for {0001} and {10$\bar{1}$0} poles, illustrated in Figure 4. A strong basal texture can be observed in the pole figures with crystallographic c-axis aligned parallel to ND and with some spread in RD. A strong peak intensity can be observed as compared to weakly textured ZEK100 consistent with literature [37].
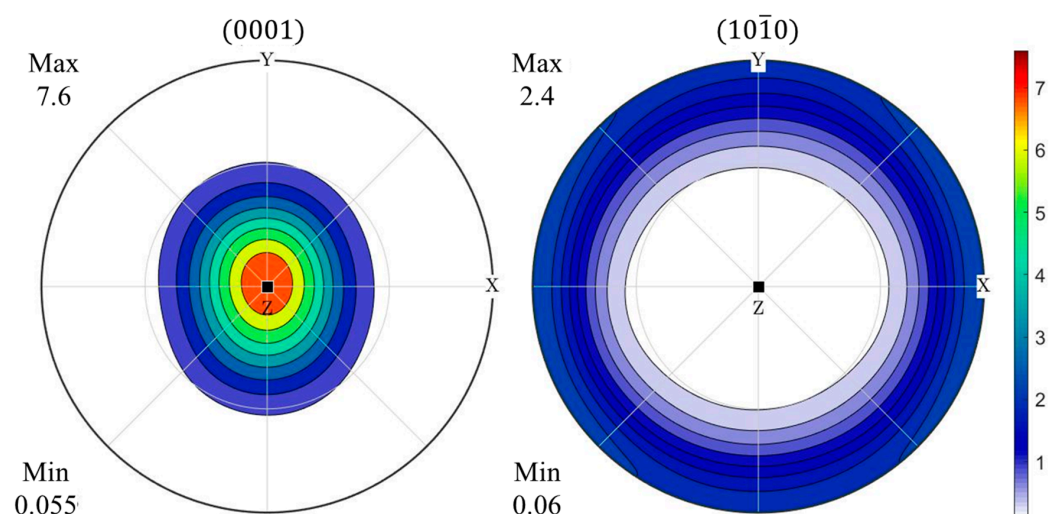

Figure 4. Initial texture for AZ31 obtained through neutron diffraction at LANL presented in {0001} and {10$\bar{1}$0} pole figure. X-axis represents TD, Y-axis represents RD and Z-axis represents ND.

All the tests were conducted in a controlled environments using an Instron 5882 testing system and a Gleeble 3500 thermomechaniocal simulator. A vacuum chamber within the Gleeble system equipped with controlled contact thermal heating was used to perform mechanical testing, with attached thermocouples providing precise temperature measurement and control. Corresponding extensometers for each system were used to measure deformation while testing, and several reruns of the tests were performed for consistency and validation. Tensile testing in ND presented a challenge as compared to the other orientations and loading directions, requiring the miniature sized sample. Specialized grips were designed in-house, depicted in Figure 3b, to hold these samples on both ends.

The mechanical response obtained from the testing is presented in Figure 5 for all twenty-four sets at different loading parameters. Since the current study aims to recreate plastic behavior in magnesium, elastic results were eliminated to display only true stress vs true plastic strain data. The summarized experimental data at different orientations, loading directions, temperatures, and strain rates can be interpreted by following the order below

1. Every graph in the figure contains tension and compression results in both RD and ND orientation tested at the same temperature and strain rate.
2. The graphs in the same rows represent test data at the same temperature, but with different strain rates for comparison. For example, figure graph (a) and (b) are both tested at 293 K, and strain rate of 0.001 s^{-1} and 0.1 s^{-1}, respectively. The testing temperature increases when reading figures from top to bottom.
3. The graphs in the left row ((a), (c), (e)) are all tested at a strain rate of 0.001 s^{-1}, and the graphs in the right row ((b), (d), (e)) are all tested at the strain rate of 0.1 s^{-1}.
4. Figures 6 and 7 provide an additional visualization for comparing experimental results at different temperatures but at the same loading orientation, direction, and strain rate of 0.001 s^{-1} and 0.1 s^{-1}, respectively.

The experimental trends agreed with the temperature-dependent behavior observed by Tan et al. [38] and the strain rate effects observed by Kurukuri et al. [39]. Basal being the predominant deformation mechanism and athermal in nature [40,41] when considering lower temperatures, the strain rate sensitivity, m is very low [38]. Strain rate sensitivity is dominated by non-basal slip systems that are more active at higher temperatures. Evidently, in Figure 5a,b, the stress–strain flow does not show prominent strain rate sensitivity at room temperature, but as the temperature increases the difference is apparent. The stress–strain results in Figure 5 show noticeable anisotropy expected of AZ31 which decreases as the temperature is increased. The anisotropy in Mg alloys arises from the fact that twinning accommodates deformation, and that c-axis deformation is polar in nature. However, twinning is athermal [42] and hence critical resolved shear stress (CRSS) required for twinning remains constant for all temperatures. Unlike twinning, dislocations are easier to activate at higher temperature. As such, the amount of twinning, and consequently the anisotropy from twinning, would be lower due to better accommodation of strain through slip. Meanwhile, higher strain rate restricts the ability of dislocation motion to accommodate overall strain. Thus twins activate more easily and propagate at extremely high velocities [43] to accommodate strain in magnesium. Increased twinning activity at higher strain rates manifests into increased anisotropy in Mg AZ31.
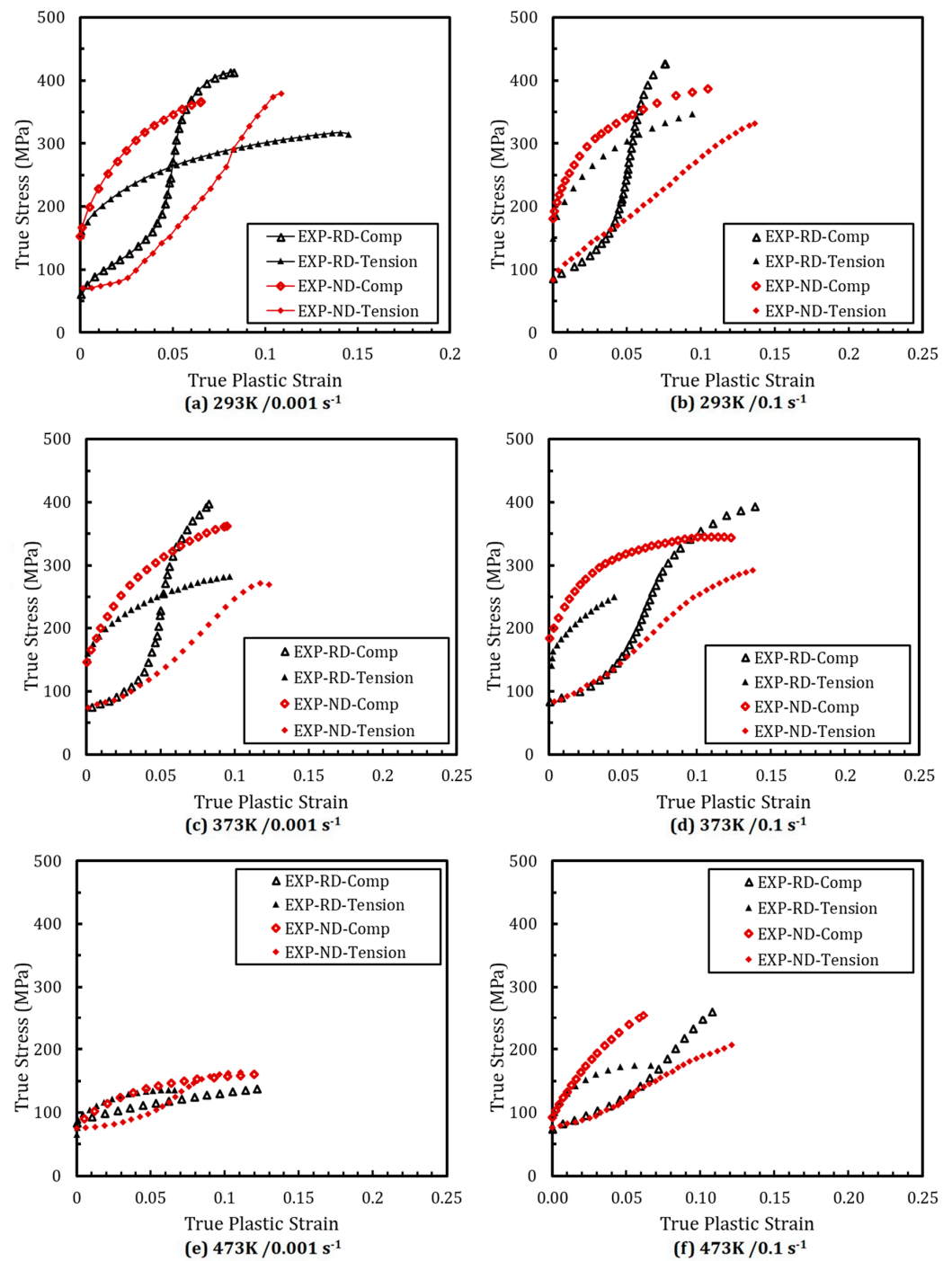
Figure 5. Stress–strain data obtained from mechanical testing AZ31 magnesium. Figures (**a**,**c**,**e**) show compression and tension results for the test conducted at 0.001 s^{-1} strain rate and temperature of 293 K, 373 K, and 473 K respectively, and figures (**b**,**d**,**f**) show compression and tension test results for 0.1 s^{-1} strain rate and temperatures of 293 K, 373 K, and 473 K, respectively.
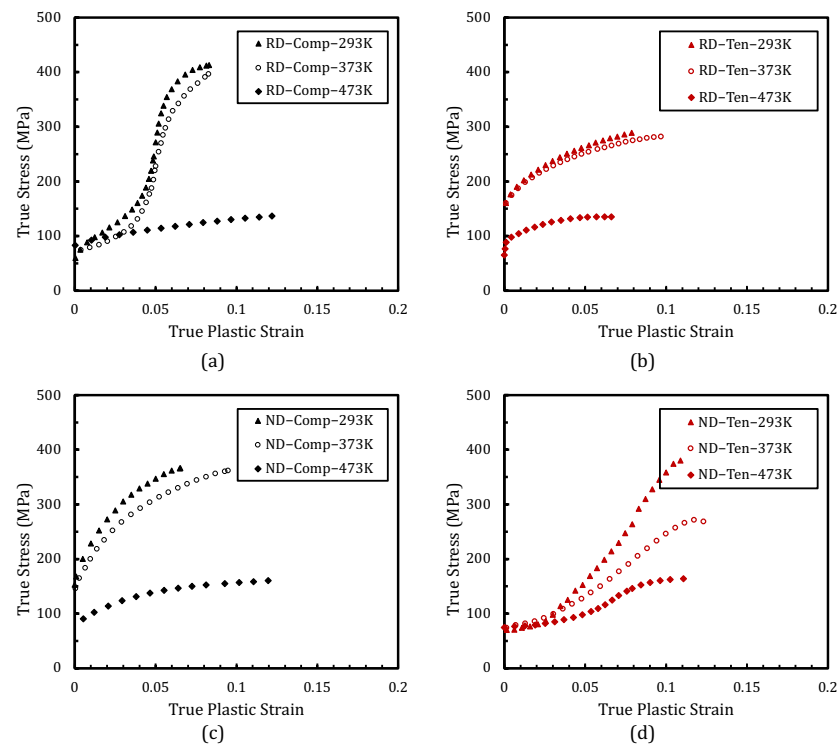
Figure 6. Stress–strain data comparison at temperatures of 293 K, 373 K, and 473 K for same loading condition and strain rate 0.001 s^{-1}. Figures (**a**,**c**) show compression results and (**b**,**d**) show tension results.
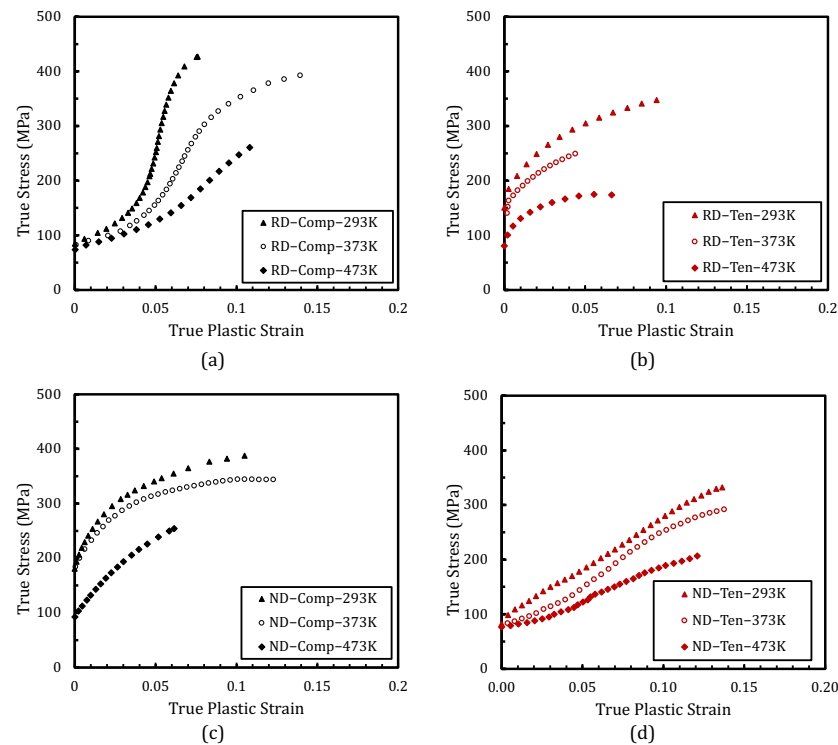

Figure 7. Stress–strain data comparison at temperatures of 293 K, 373 K, and 473 K for same loading condition and strain rate 0.1 s^{-1}. Figures (**a**,**c**) show compression results and (**b**,**d**) show tension results.

2.2. Weakly Textured Magnesium ZEK100

Weakly textured ZEK100 magnesium alloy (1% Zn, 0.1% Zr, 0.1% RE) was chosen as the second alloy for study because twinning is comparatively sparse in the grains, and the texture shows fewer autocatalysis phenomena. As such, slip and twinning more equally dominate plasticity, considering not all grains are twinning in a material with weak texture. Compared to a strongly textured alloy that has almost all the grains twinning, more slip-twin interaction can be expected as some grains twin while some do not have twins and have slips.

Thin sheets of Mg ZEK100 were tested in tension to failure at temperatures of 25 °C, 100 °C, and 200 °C to obtain stress–strain data. Square sheets of average dimension 30 cm × 30 cm, and 2 mm in thickness, were sampled to cut in 0°, 30°, 60°, and 90° (transverse direction (TD)) angle with reference to RD. The above is summarized in the test matrix presented in Table 1. The sample geometry as in Figure 8, was created after referring to the ASTM standards and Gleeble specimen sample drawings. The samples were tested in a controlled environment, using contact thermal heating for higher temperature testing in tension at a 0.001 s^{-1} strain rate. Extensometer was used for better precision in data collection, and experiments were performed for twelve different sets of testing conditions.
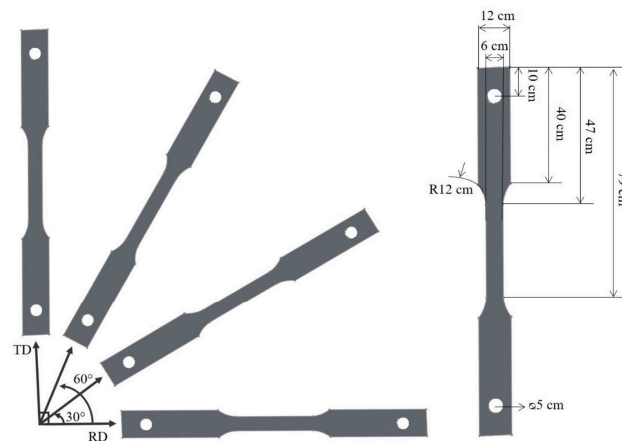

Figure 8. Dimensions of a flat dog bone specimen obtained from a 2 mm thin sheet of ZEK100, designed using ASTM standards and Gleeble sample drawing. The sample was cut in 0° (RD), 30°, 60°, and 90° (TD) orientations.

The texture data for ZEK100 was obtained through an X-ray diffraction (XRD) performed a Rigaku SmartLab system with a Cu Kα target. The pole graphs in $\{0001\}$ and $\{10\bar{1}0\}$ are plotted below in Figure 9, evident of weak basal texture and weak peak intensity when compared to AZ31 in Figure 4. Most of the grains in ZEK100 have their c-axis aligned perpendicular to the RD with some tilting perpendicular to the TD thus, a more distributed texture is obtained.

Experimentally obtained results are compiled in Figure 10 on true stress vs true plastic strain graph tested in different loading orientations in tension at the strain rate of 0.001 s^{-1}. Each graph represents test data from experiments conducted at 293 K, 373 K, and 473 K, respectively. The acquired experimental data is in agreement with the data presented on commercial grade ZEK100 in work by Kurukuri et al. [44]. Their work highlights the in-plane anisotropy exhibited by ZEK100 with specimen loaded in 90° (TD) showing the lowest yield strength and highest in 0° (RD). Hardening difference can also be observed, with TD hardening more as compared to RD.
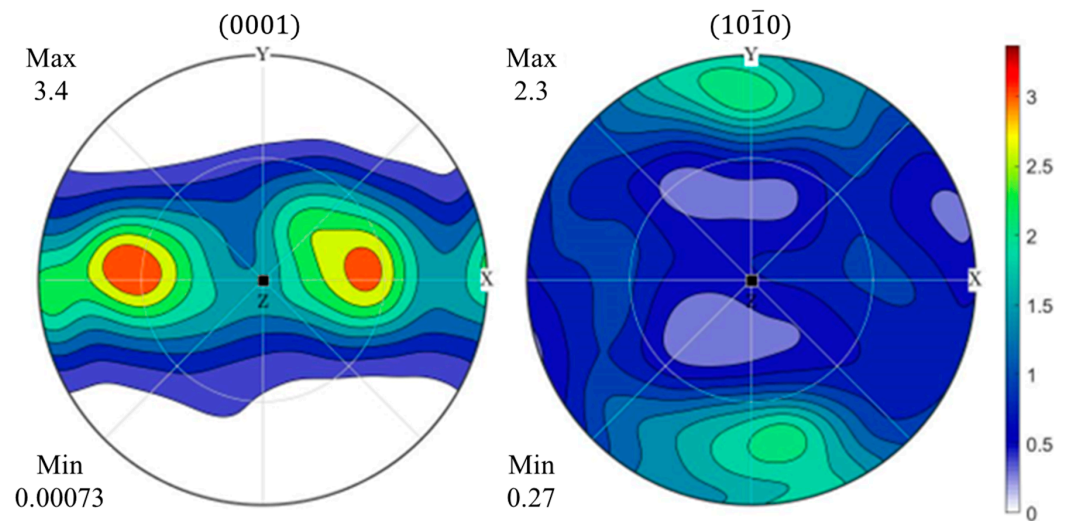
Figure 9. Initial texture for ZEK100 obtained using X-ray diffraction (XRD) scan presented in $\{0001\}$ and $\{10\bar{1}0\}$ pole figure. X-axis in the plot is TD and Y-axis is RD.
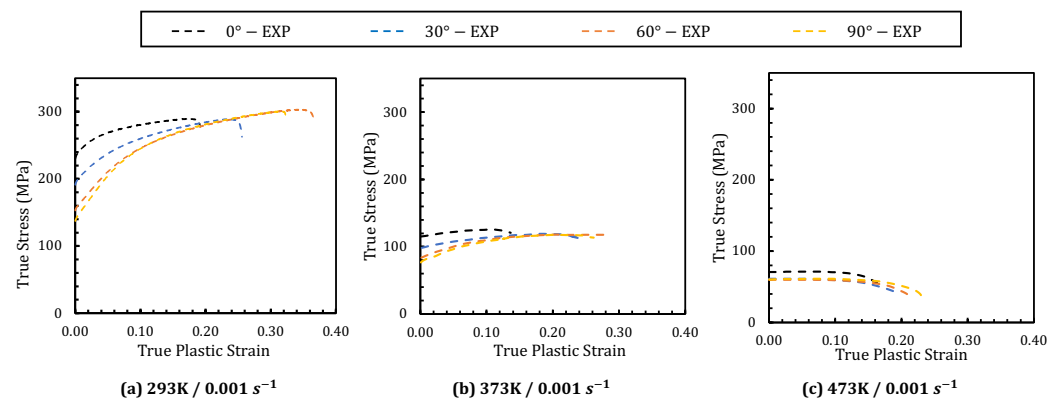

Figure 10. Stress–strain data comparison at temperatures of 293 K (**a**), 373 K (**b**), and 473 K (**c**) for same loading condition and strain rate 0.001 s^{-1}.

It has been predicted that magnesium alloys with more randomized basal texture would provide better formability at room temperature. The addition of the rare earth metals to Mg alloys has shown a weakening texture with reduced basal pole intensity proving to be more ductile at room temperature and less anisotropic when compared to the traditional Mg. Magnesium alloy like ZEK100 that have rare earth as part of composition exhibit a texture called "RE texture" that shows a distributed basal texture with some $\langle c \rangle$-axis inclining toward the TD [45–47]. The stress–strain results obtained from experimentation are a reflection of the initial texture obtained from the raw material. A weak texture and split intensity favoring inclination towards TD helps basal and extension twin to activate resulting in three times higher ductility as compared to the RD [48]. Compared to AZ31, ZEK100 shows higher in-plane anisotropy with yield stress in tension RD exceeding tension TD by approximately 100 MPa [49]. Tension in RD results in much higher yield strength as non-basal slip systems are active requiring higher critical stress but exhibit low ductility contrary to TD which demonstrates higher elongation. ZEK100 has the highest hardening when strained in RD and decreases as the orientation angle increases with tension in TD having the lowest hardening. The in-plane anisotropy of the material decreases drastically with the increase in temperature. Generally, at room temperature a combination of easy slip systems of basal $\langle a \rangle$ and twin systems are active depending on the loading orientation, but at higher temperatures non-basal slip systems operate easily thus, decreasing anisotropy

is observed as the temperature increases [38]. The chances of twin activating at higher temperature would be reduced thus, reducing the associated anisotropy.

3. Crystal Plasticity Simulation and Discussion

3.1. Incorporating Dislocation Transmutation Scheme in VPSC Dislocation-Density Model

In the current study, VPSC code with dislocation density-based model, incorporated with transmutation scheme has been used. A framework was created by Allen et al. [36] to incorporate the transmutation scheme in VPSC and to simulate the mechanical behavior of pure Mg. In the previous work, VPSC simulation results with the incorporation of transmutation scheme showed good agreement with the stress–strain response compared to the results incorporating twin storage factor [36]. Equation (26) was further modified to introduce a non-dimensional term η, indicating the amount of dislocation density that failed to transmute and were lost to disassociation.

$$d\rho^{iTF}(V) = \frac{V^T \rho^{iT} + dV \sum_j (1 - \eta_j)\alpha_{ij}\rho^{jP}}{V^T + dV} \tag{27}$$

An extra row was added to the transmutation matrix α_{ij}, to account for sessile and higher-order dislocations. The calculation for the correspondence matrix mapping the slip systems in the parent matrix to the reformed slip system in the twin volume is elaborated in Niewczas's work [50]. The transmutation matrix was calculated only for the $\{10\bar{1}2\}$ tension twin, as $\{10\bar{1}1\}$ compression twins are assumed to have negligible contribution to transmutation, requiring high strain to activate and rushing damage. The elements in the transmutation matrix are calculated using the following equation,

$$\alpha_{ij} = \frac{n_j^C}{n_j^{tot}} \tag{28}$$

Here n_j^C is the number of slip systems in the parent volume that are mapped onto the *i*th slip mode in the twin volume fraction, and n_j^{tot} is the total number of *j*th type slip modes present in the parent matrix. Below is the matrix used in this study from [36].

$$\alpha_{ij} = \begin{bmatrix} 0.0 & 0.3333 & 0.3333 \\ 0.3333 & 0.0 & 0.0 \\ 0.6666 & 0.0 & 0.0 \\ 0.0 & 0.6666 & 0.6666 \end{bmatrix}$$

The detailed molecular dynamic study conducted by El Kadiri et al. [51] infers the fate of the dislocation interacting with the twin boundary depending upon the type of dislocation and its orientation when interacting with the twin. Taking this study into consideration, Allen et al. [36] modified the VPSC code to allow for screw type basal dislocations to completely transmute when obstructed by a twin boundary. Edge type dislocations can transmute across the twin boundary if they have a positive orientation with respect to the twin boundary or form twin disconnections if they have a negative orientation. The non-dimensional η term that accounts for the number of dislocations that have been disassociated is set to 0.5 for all the slip modes.

The five deformation modes used in the study are basal $\langle a \rangle$ ($\{0001\}\langle 1\bar{2}10\rangle$) and prismatic $\langle a \rangle$ ($\{10\bar{1}0\}\langle 1\bar{2}10\rangle$), providing deformation along the close-packed direction, second order pyramidal $\langle c + a \rangle$ ($\{11\bar{2}2\}\langle \bar{1}\bar{1}23\rangle$), capturing slip along non-basal direction and tension twin ($\{10\bar{1}2\}\langle 10\bar{1}1\rangle$) and compression twin ($\{10\bar{1}1\}\langle 10\bar{1}2\rangle$) known to contribute to hardening and failure in magnesium. The slip and the twin modes are summarized in Table 2.

Table 2. Slip and Twinning modes for magnesium used in VPSC simulation.

Symbol	Mode	Crystallography	No. of Systems	b (nm)
$\alpha = 1$	Prismatic $\langle a \rangle$	$\{10\bar{1}0\}\frac{1}{3}\langle\bar{1}2\bar{1}0\rangle$	3	0.321
$\alpha = 2$	Basal $\langle a \rangle$	$\{0001\}\frac{1}{3}\langle2\bar{1}\bar{1}0\rangle$	3	0.321
$\alpha = 3$	Pyramidal $\langle c + a \rangle$	$\{11\bar{2}2\}\frac{1}{3}\langle\bar{1}\bar{1}23\rangle$	6	0.612
$\beta = 1$	Tensile Twin	$\{10\bar{1}2\}\langle10\bar{1}1\rangle$	6	0.138
$\beta = 2$	Compression Twin	$\{10\bar{1}2\}\langle10\bar{1}1\rangle$	6	0.0924

b: Burgers vector.

The VPSC simulation were performed on 24 scenarios for Mg AZ31 alloy and 12 scenarios in Mg ZEK100 alloy. The orientation distribution function obtained using texture information, as shown in previous section (Figures 4 and 9), were used to generate input orientation for VPSC simulation. Likewise, one set of parameters were used for all scenarios of each Mg alloys except for $\tau_0^\alpha(temp)$, which is a function of temperature. For calibration of parameter, a MATLAB [52] script was used to run all scenarios for each alloy and calculate mean squared error (MSE) comparing with experimental data. A gradient descent method was used to get the optimum parameters minimizing summed error for all case scenarios in each alloys. The results discussed in upcoming subsections utilizes the optimum parameters that resulted in minimum summed MSE from all scenarios for each alloys and the calibrated parameters are shown in Tables 3–6.

Table 3. Prismatic, basal, and pyramidal dislocation density hardening parameters for magnesium AZ31.

Parameters	Prismatic ($\alpha = 1$)	Basal ($\alpha = 2$)	Pyramidal $\langle c + a \rangle$ ($\alpha = 3$)
$k_1\,(m^{-1})$	0.25×10^9	0.425×10^9	1.30×10^9
$\dot{\varepsilon}_0\,(s^{-1})$	1.00×10^7	1.00×10^7	1.00×10^7
g^α	0.0037	0.0037	0.007
D_0^α (MPa)	15×10^3	6×10^3	1×10^3
τ_0^α (MPa) (293 K)	84	26	130
τ_0^α (MPa) (373 K)	75	24	110
τ_0^α (MPa) (473 K)	30	15	45
q^α	0	0	0
X	0.9	0.9	0.9
HP^α	0	0	0
$HP^{\alpha\beta}$	0	0	0

α: slip mode. k_1: coefficient for dislocation generation. g^α: effective activation enthalpy. D_0^α: drag stress. τ_0^α: initial critical stress value. q^α: rate coefficient defining the fraction of recovered dislocation stored as debris. χ: dislocation interaction coefficient between 0.1 and 1.0. HP: Hall-Petch.

Table 4. Tension and compression twin dislocation density hardening parameters for magnesium AZ31.

Parameters	Tension Twin ($\beta = 1$)	Compression Twin ($\beta = 2$)
τ_{crit} (MPa) (293 K)	31	225
τ_{prop} (MPa) (293 K)	5	225
τ_{crit} (MPa) (373 K)	31	200
τ_{prop} (MPa) (373 K)	5	200
τ_{crit} (MPa) (473 K)	31	120
τ_{prop} (MPa) (473 K)	5	120

β: twin mode. τ_{crit}: critical stress for twin. τ_{prop}: critical stress for twin propagation.

Table 5. Prismatic, basal, and pyramidal dislocation density hardening parameters for magnesium ZEK100.

Parameters	Prismatic ($\alpha = 1$)	Basal ($\alpha = 2$)	Pyramidal $\langle c + a \rangle$ ($\alpha = 3$)
$k_1 \left(m^{-1} \right)$	0.2×10^9	0.65×10^9	0.1×10^9
$\dot{\varepsilon}_0 \left(s^{-1} \right)$	1.00×10^7	1.00×10^7	1.00×10^7
g^α	0.0035	0.0035	0.007
D_0^α (MPa)	5×10^3	1.1×10^3	5×10^3
τ_0^α (MPa) (293 K)	136	56	200
τ_0^α (MPa) (373 K)	75	27	80
τ_0^α (MPa) (473 K)	45	15	50
q^α	0	0	0
X	0.9	0.9	0.9
HP^α	0	0	0
$HP^{\alpha\beta}$	0	0	0

α: slip mode. k_1: coefficient for dislocation generation. g^α: effective activation enthalpy. D_0^α: drag stress. τ_0^α: initial critical stress value. q^α: rate coefficient defining the fraction of recovered dislocation stored as debris. χ: dislocation interaction coefficient between 0.1 and 1.0. HP: Hall-Petch.

Table 6. Tension and compression twin dislocation density hardening parameters for magnesium AZ31.

Parameters	Tension Twin ($\beta = 1$)	Compression Twin ($\beta = 2$)
τ_{crit} (MPa) (293 K)	50	250
τ_{prop} (MPa) (293 K)	25	250
τ_{crit} (MPa) (373 K)	50	100
τ_{prop} (MPa) (373 K)	25	100
τ_{crit} (MPa) (473 K)	50	60
τ_{prop} (MPa) (473 K)	25	60

β: twin mode. τ_{crit}: critical stress for twin. τ_{prop}: critical stress for twin propagation.

3.2. Simulation Results for Magnesium AZ31

Studies [4,53] have been conducted on AZ31 that use the Voce-type hardening model and a latent hardening term for hardening encountered during twinning to model the temperature dependency. Ardeljan et al. [54] conducted a study using the VPSC dislocation density-based model but used the Hall-Petch effect to model the hardening in the grain associated with dislocations encountering the twin. Hardening parameters from these studies were used as basics to fit the experimental curves. The hardening parameters that provided a reasonable fit for all the experimental data at various conditions for the five deformation modes are summarized in Tables 3 and 4. In the current study, the initial critical stress ratio for basal $\langle a \rangle$ to prismatic $\langle a \rangle$ to second-order pyramidal $\langle c + a \rangle$ to the tension twin at room temperature is 1:3.2:5:1.2, which is closer to the values found by Jain and Agnew [4] at 1:3.2:5:1.5 versus the ratio of 1:4.1:14:1.2 reported by Ardeljan et el. [54]. The initial stress for tension twin is picked to be very close to the stress value of basal $\langle a \rangle$ and will remain same with the change in temperature due to its athermal nature.

The temperature sensitivity for the five deformation systems can be observed to be different. Basal, which is the dominant deformation mechanism, has low sensitivity to temperature change followed by prismatic showing a higher dependency on temperature. The second-order pyramidal slip that accommodates $\langle c \rangle$-axis deformation shows the highest sensitivity to temperature changes. Thus, deformations relying on basal activity would be less sensitive to temperature, and deformations with predominant pyramidal would be highly sensitive to temperature changes.

Mechanical twinning is athermal in nature [42], meaning it is not sensitive to temperature changes. Hence, the same parameters were used for the critical stress and stress for twin propagation over all the temperature range. From the hardening parameters for tension and compression twinning, tension twin propagates early due to its CRSS being lower than that of second-order pyramidal, assisting in accommodating $\langle c \rangle$-axis deformation but

also contributing to hardening. Compression twin requires a high CRSS to propagate and causes immediate damage.

To fit the hardening parameters, the stress–strain response at room temperature for compression in RD and compression in ND was used to derive the hardening parameters as profuse twinning would be present in compression RD, resulting in a steep hardening curve. Allen et al. [36] demonstrated in their work, the difference in saturation stress in IPC and TTC to be a result of hardening due to higher dislocations forming during transmutation. This knowledge was used to make fitting the flow response easier by turning off transmutation ($\eta = 1$) and fitting compression ND and the initial curve for compression RD. Subsequently, transmutation was permitted by 50% ($\eta = 0.5$) to fit the saturation stress for compression in RD. The additional stress–strain plots were then fit in the order of temperature, from 293 K to 373 K, and lastly 473 K by calibrating the initial critical stress parameter, τ_0 for all slip modes and critical and twin propagation stress for compression twin.

The simulation fit to the experimental data derived using the VPSC model with the hardening parameters listed in Tables 3 and 4 yields the results presented in Figure 11 for strain rate 0.001 s^{-1} and Figure 12 for strain rate 0.1 s^{-1}. Subplots (a) and (b) at both the strain rates show stress–strain plots at room temperature and have captured the anisotropy in ND vs RD adequately well. As discussed in the earlier section low room temperature strain rate sensitivity is observed in AZ31 which has been well captured in the simulation. A similar trend is observed for stress–strain subplots (c) and (d) at both the strain rates, simulated at temperature 393 K. Prominent ductility is observed in magnesium as the temperature increases from 373 K to 473 K and relative anisotropy is low in subplots (e) and (f). However, the simulation results showed limitation predicting stress–strain response for RD compression at low strain rate of 0.001 s^{-1}. While experimental data showed no plateau region from profuse twinning, the simulation results clearly shows plateau effect that arises from profuse twinning. Similar effects were observed previously with over-prediction of profuse twinning by VPSC model resulting in plateau region for higher temperature [23].

As compared to Zr [30], low initial yield anisotropy is observed in AZ31 between the TTC and IPC direction which can be attributed to the availability of basal $\langle a \rangle$ slip systems which have a lower Schmid factor as compared to pyramidal $\langle a \rangle$ which is the easy slip system in Zr. The modal activity of each slip and twin mode in the parent grain and the primary twin is plotted in Figure 13 for simulation results at room temperature and quasi-static strain rate. Similar activity was seen in room temperature simulation at 0.1 s^{-1} strain rate. The activity trend for the slip and twin modes is similar to the trend observed in AM30 [55], pure magnesium [13], and AZ31 [54].

These results are consistent with existing findings, as when compressed in RD (IPC) ((a), (b)) and pulled in tension in ND (TTT) ((g), (h)), basal is the easiest deformation system available along with tension twin which propagated early due to low CRSS and accommodates $\langle c \rangle$-axis deformation in absence of non-basal slips. The sigmoidal curve which is a characteristic of in-plane compression has been associated with the extension twin, causing huge strain hardening and dissipating with the increase in strain [56]. The model has been able to capture this behavior well and the tension twin activity can be seen in the parent grain. Activity in the twin fraction is seen in these loading conditions ((b), (h)) due to twin-slip interactions and as Hall-Petch effects are neglected in this study, the transmutation scheme has captured the slip-twin interactions well. Basal being the easiest slip system is also easily activated when compressing in ND ((c), (d)), and pulling in tension in RD with minimal twin activity. The higher yield stress requirements in these directions and loading conditions are a result of the non-basal slip systems being active reflective in the activity obtained from the simulations.
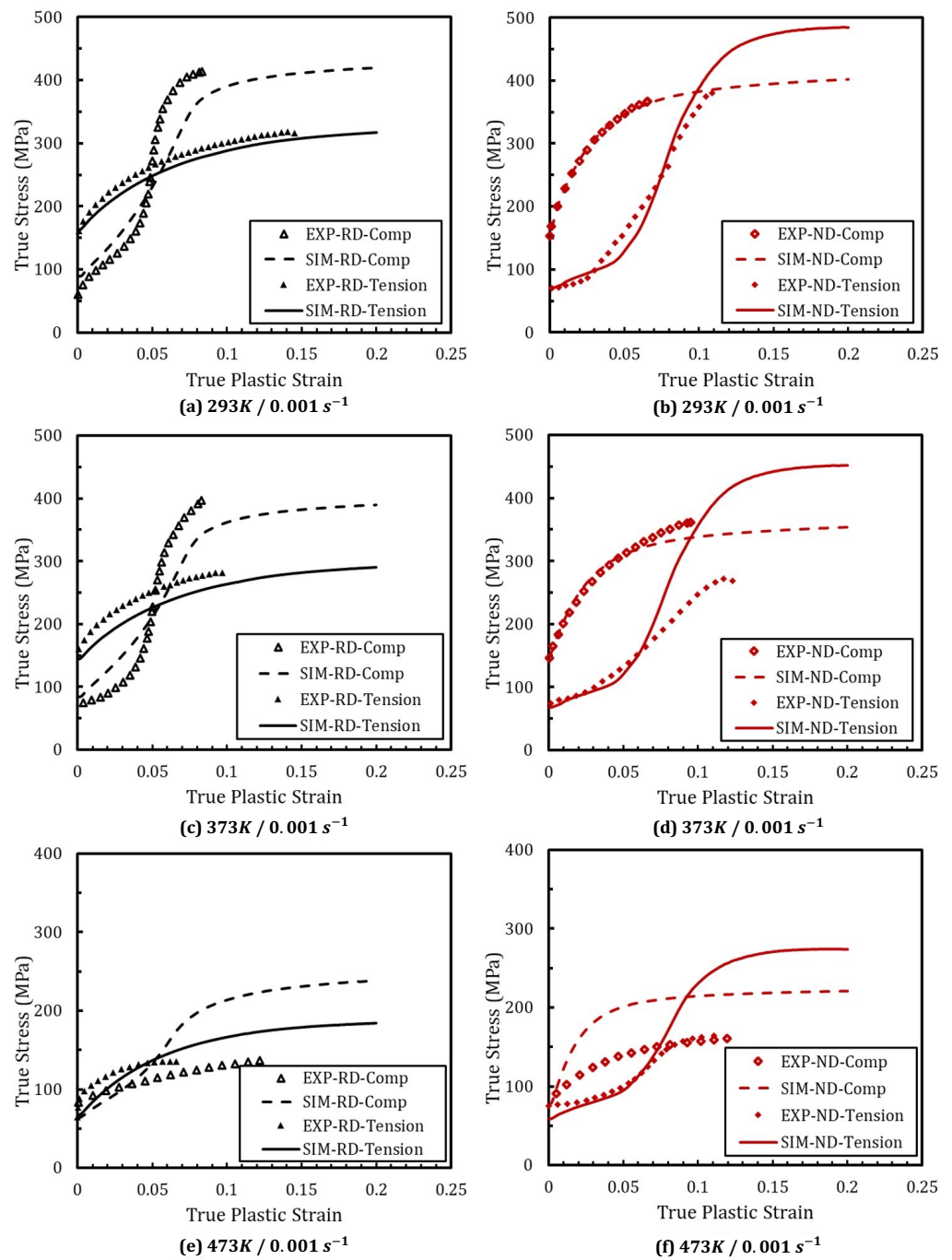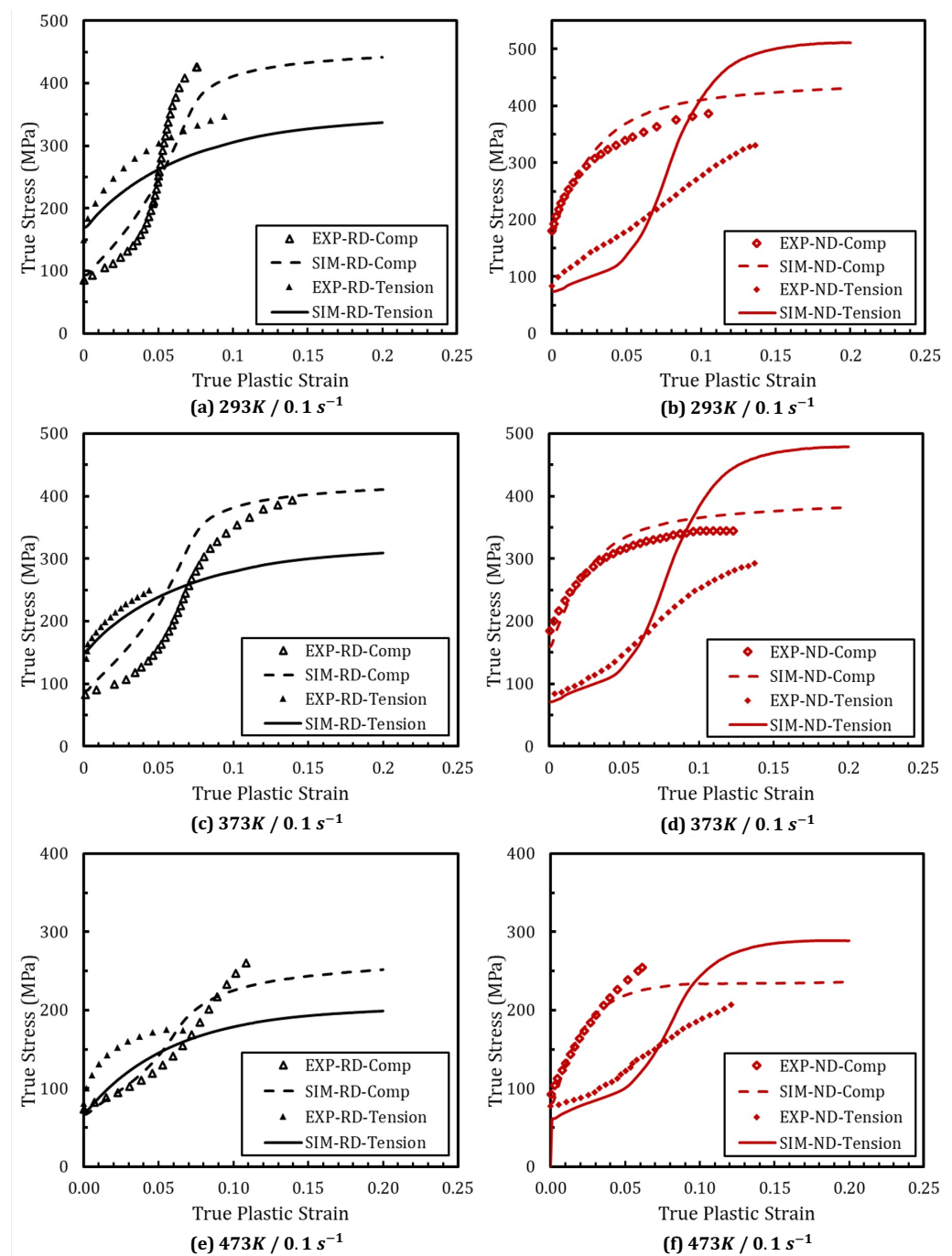
Figure 11. Stress–strain response comparing the experimental and simulation in Compression and tension at the strain rate of 0.001 s^{-1}. (**a**) RD at 293 K (**b**) ND 293 K (**c**) RD at 373 K (**d**) ND at 373 K (**e**) RD at 473 K (**f**) ND at 473 K.

Figure 12. Stress–strain response comparing the experimental and simulation in Compression and tension at the strain rate of 0.1 s^{-1}. (**a**) RD at 293 K (**b**) ND 293 K (**c**) RD at 373 K (**d**) ND at 373 K (**e**) RD at 473 K (**f**) ND at 473 K.

The asymmetry in AZ31 between the tension and compression loading and the out-of-plane asymmetry is still a very noticeable phenomenon at higher temperatures though it is relatively lower as compared to room temperature. This suggests that the CRSS of the non-basal slip systems are still higher than that of tension twinning at the higher temperature [57]. As the temperature increases, more non-basal slip systems are readily available, and less strain hardening is observed. The strain rate sensitivity differs drastically for AZ31 as the temperature increases from RT to 473 K. Previous studies have shown the rate sensitivity increases 15 times with m ranging from approximately 0.01 to 0.15 as the temperature is increased from RT to 473 K [6]. The yield strength at different

strain rates for compression in RD is observed to be similar considering twinning is an important mechanism in RD compression which is known to be rate insensitive, or when compressing in ND where pyramidal twinning and tensile twins are dominant [57]. All of these characteristics are successfully captured by the simulation results.
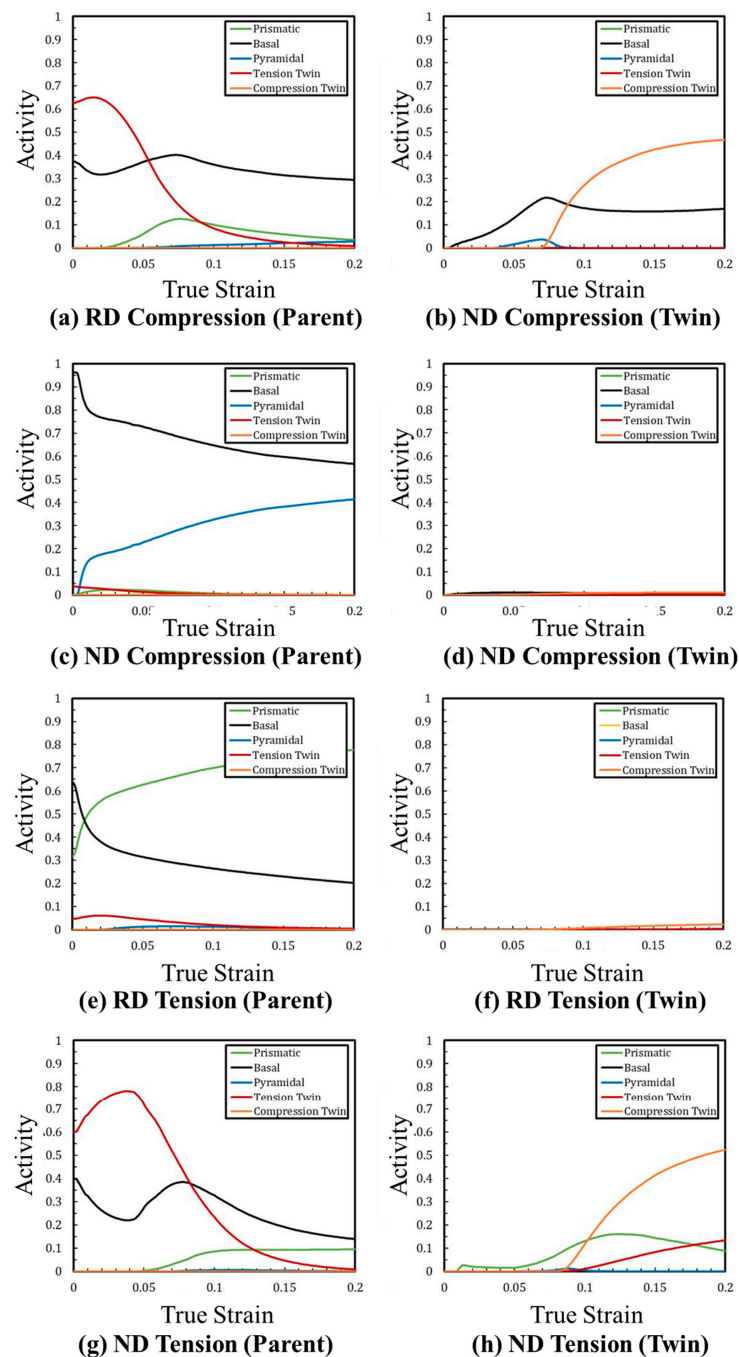

Figure 13. Activity of slip and twin within the parent (**a,c,e,g**) and primary twin (**b,d,f,g**) obtained from the simulations of AZ31 at room temperature (293 K) and 0.001 s^{-1} strain-rate. Subplots (**a–d**) show compression activity and (**e–h**) show tension activity. RD is in-plane and ND is thru-thickness.

The texture data obtained from the simulation in tension and compression in both RD and ND at room temperature and quasi-static strain rate is presented in the form of $\{0001\}$ and and $\{10\bar{1}0\}$ pole figures in Figure 14. Experimental texture data was not available for comparison, but the pole figures show similarity to deformed texture in other magnesium

work [4,13,49,55]. The undeformed texture suggests that the crystals are oriented with $\langle c \rangle$-axis normal to the sheet surface with a little tilt towards the RD when viewed for $\{0001\}$ pole figure Figure 4. The deformation from loading in compression in RD has caused all the crystals to reorient and move parallel to the loading direction, a signature of twinning. The basal planes are rotated by 86° because of the extension twin activating early on aligning the $\langle c \rangle$-axis of the crystals to the loading direction [49]. The deformed texture in Figure 14c for tension in RD, shows the basal planes rotate to lie parallel to the sheet surface and the tensile axis suggesting basal slip dominated deformations and twinning that has led to the rotation of lattice. The effects of lattice rotation can be seen in $\{10\bar{1}0\}$ pole graphs where the intensity maxima are uniformly separated from each other at the peripheral of the stereographic projection. Compressing in ND increases the intensity of the basal texture as the material deforms primarily by basal and pyramidal. Whereas when loaded in tension in ND a complete reorientation of the basal texture is observed with the intensity maxima split in the in-plane rolled direction that has caused due to the presence of twinning. The $\{10\bar{1}0\}$ pole figure shows the presence of prismatic oriented perpendicular to the ND while the original texture was pure basal texture and pyramidal planes were parallel to ND. Similar texture evolution as room temperature is observed at higher temperatures with decreasing basal pole intensity as the temperature increases which is due to less twinning activity and more slip deformation mode availability, and an increase in intensity is observed with similar texture for the same temperature but a higher strain rate.

3.3. Simulation Results for Magnesium ZEK100

Magnesium alloy ZEK100 was chosen as one of the study materials due to its weak texture, which as predicted did not show strong anisotropy as compared to the strongly textured AZ31. Previous studies on ZEK100 have used the EVPSC model to simulate the stress–strain behavior for in-plane anisotropy and VPSC model with minimum parameter approach to predict the texture evolution [58], but a compressive study to model the anisotropy at different temperatures is yet to be published. The hardening parameters for pure magnesium in work by Oppedal et al. [13] were used as a basis for modeling the room temperature stress–strain response in all four orientations (0°, 30°, 60°, 90°). Once satisfactory hardening parameters were achieved at room temperature, the hardening parameters were calibrated for stress–strain data at 373 K and 473 K temperatures. The fit to the experimental tensile stress–strain response in 0° (RD), 30°, 60°, and 90° (TD) at temperatures of 293 K, 373 K, and 473 K for 0.001 s^{-1} strain rate, yield the hardening parameters listed in Tables 5 and 6. Compared to AZ31, very high initial critical stress was used to activate the slip and the twin modes, and easy slip systems of basal $\langle a \rangle$ and prismatic $\langle a \rangle$ readily available for deformation. A very high critical value for the tension twin was determined, and the same hardening parameter was used at all temperatures due to the athermal nature of the tension twin.

A good simulation fit was achieved to the stress–strain response using the hardening parameters as can be seen in Figure 15. The parent grain activity and activity in the twin are depicted in Figure 16 for all orientations at room temperature. Tension twins are sparsely present in RD, but the activity within the twin increases as the orientation is changed, moving from RD towards ND, with ND having maximum tension twin activity and interactions within the twin. This explains the increase in hardening observed in the stress–strain data as the orientation changes from RD to TD. It is evident that because the texture is distributed and not all $\langle c \rangle$-axis are oriented in one direction, basal $\langle a \rangle$ and prismatic $\langle a \rangle$, which are the easy slip systems are readily available for deformations regardless of the orientation as observed in the activity in the parent grain.
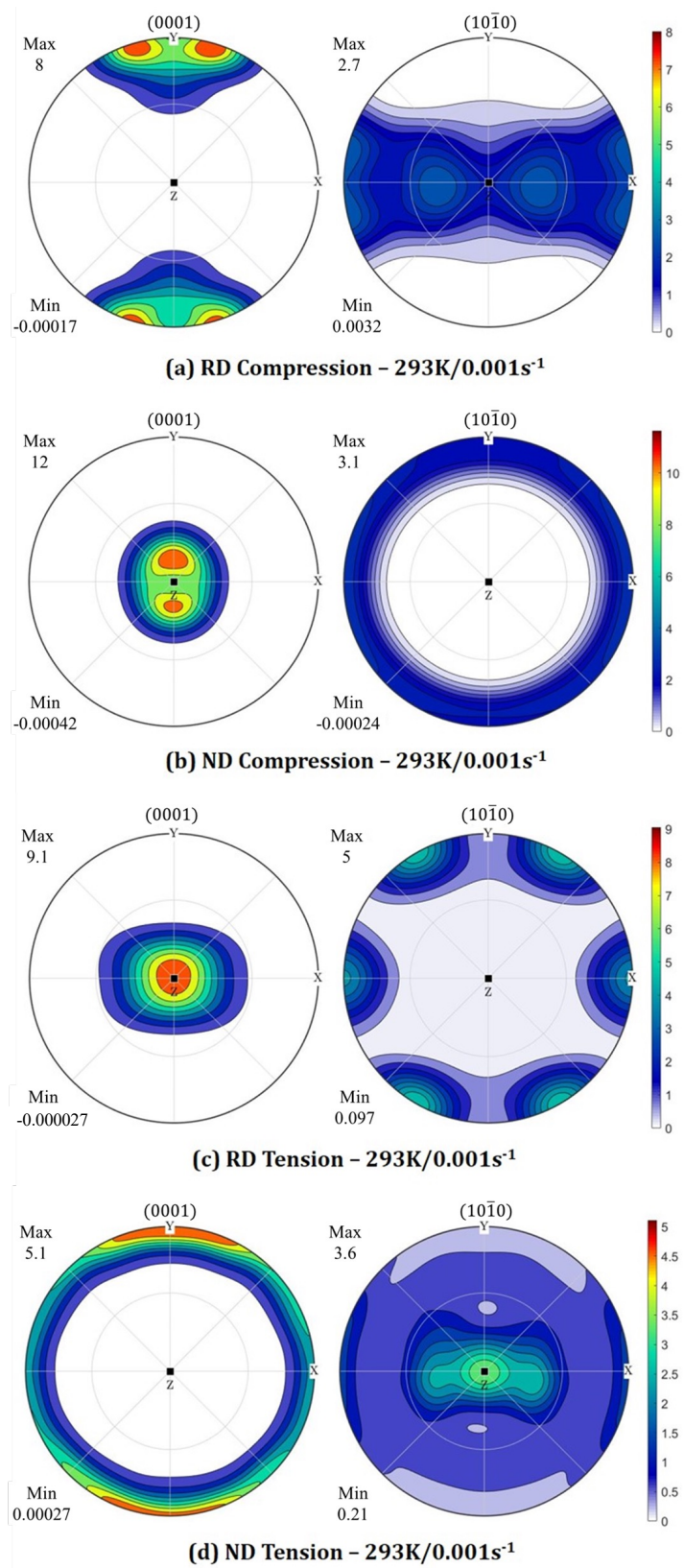
Figure 14. Texture pole figure for $\{0\,0\,0\,1\}$ and $\{1\,0\,\bar{1}\,0\}$ at failure obtained from simulation for tension and compression in both ND and RD at room temperature and 0.001 s^{-1} strain rate. The X-axis represents TD, Y-axis represents RD and Z-axis represents ND.

Despite the weak texture of the ZEK100, a characteristic of the materials with the addition of RE-elements in Mg, in-plane anisotropy in ZEK100 is present. Due to the variation in texture and high Schmid factor, basal $\langle a \rangle$ and extension twin $\{10\bar{1}2\}\langle10\bar{1}1\rangle$ easily activate in TD (90°) as the basal texture is dispersed with some inclination towards TD. This can be observed in Figure 16g parent grain, where high tension twin activity can be observed initially until other non-basal slip systems are eventually activated as the material is strained. Subsequent activity within the primary twin is also observed in the plot (h). Localized twin bands that are generally observed in Mg alloys are more uniformly distributed in the case of ZEK100 owing to its randomized texture [48]. The current model was successful in capturing the low yield and high ductility in TD. An almost perfect simulation fit for the stress–strain response is obtained for tension in 30° and 60° whose activity files show a reduction in twin activity as the orientation moves towards RD. Prismatic $\langle a \rangle$ is seen to be more readily available as the twin activity reduces, along with the easy slip system, basal $\langle a \rangle$. RD demonstrating high yield stress and plastic deformation only accommodated by the slip systems. The high yield strength observed in RD suggests that the yielding was a result of prismatic $\langle a \rangle$ rather than basal $\langle a \rangle$ which has a very low CRSS and is reflected in the parent activity in plot (a) of Figure 16. The slip and twin activity present in this work are consistent with the prediction derived using an VPSC model by Ge [23,59].

The texture evolved at failure for tension in 0° and 90° is presented in Figure 17. The texture for 0° does not show much difference in the initial and the final texture other than an increase in intensity at the slip maxima Figure 9. The initial texture had no $\langle c \rangle$-axis aligned parallel to RD and similar is observed in the final texture which is consistent with the results obtained in work by Kurukuri et al. [44]. Contrary to results in RD, the texture in TD goes through major reorientation as the grains that were initially aligned in TD have now moved in alignment with TT and RD. This reorientation can be credited to the activity of the twin when strained in TD. Overall, the simulation has provided a good prediction for stress–strain and texture evolution for ZEK100.
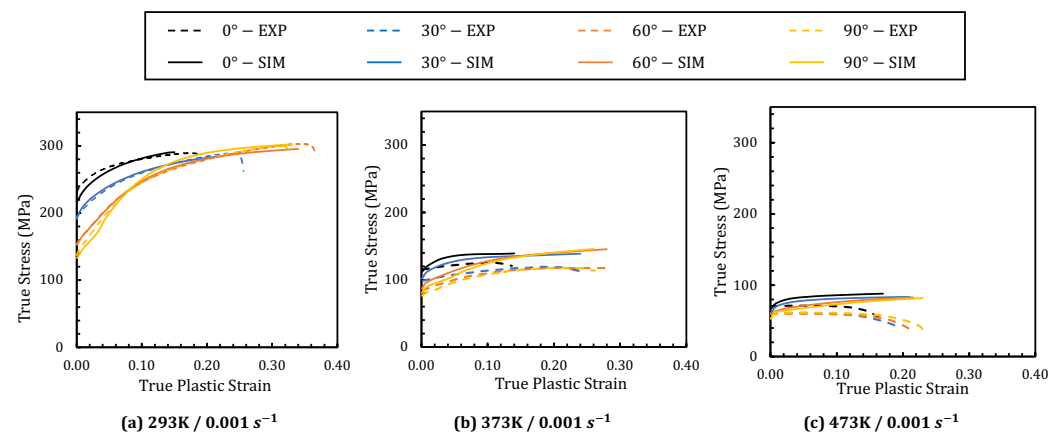

Figure 15. Stress–strain response of ZEK100 in tension and the simulation data fit achieved using the VPSC dislocation density model. Subplots (**a**–**c**) are tests and simulations conducted at 293 K, 373 K, and 473 K, respectively.
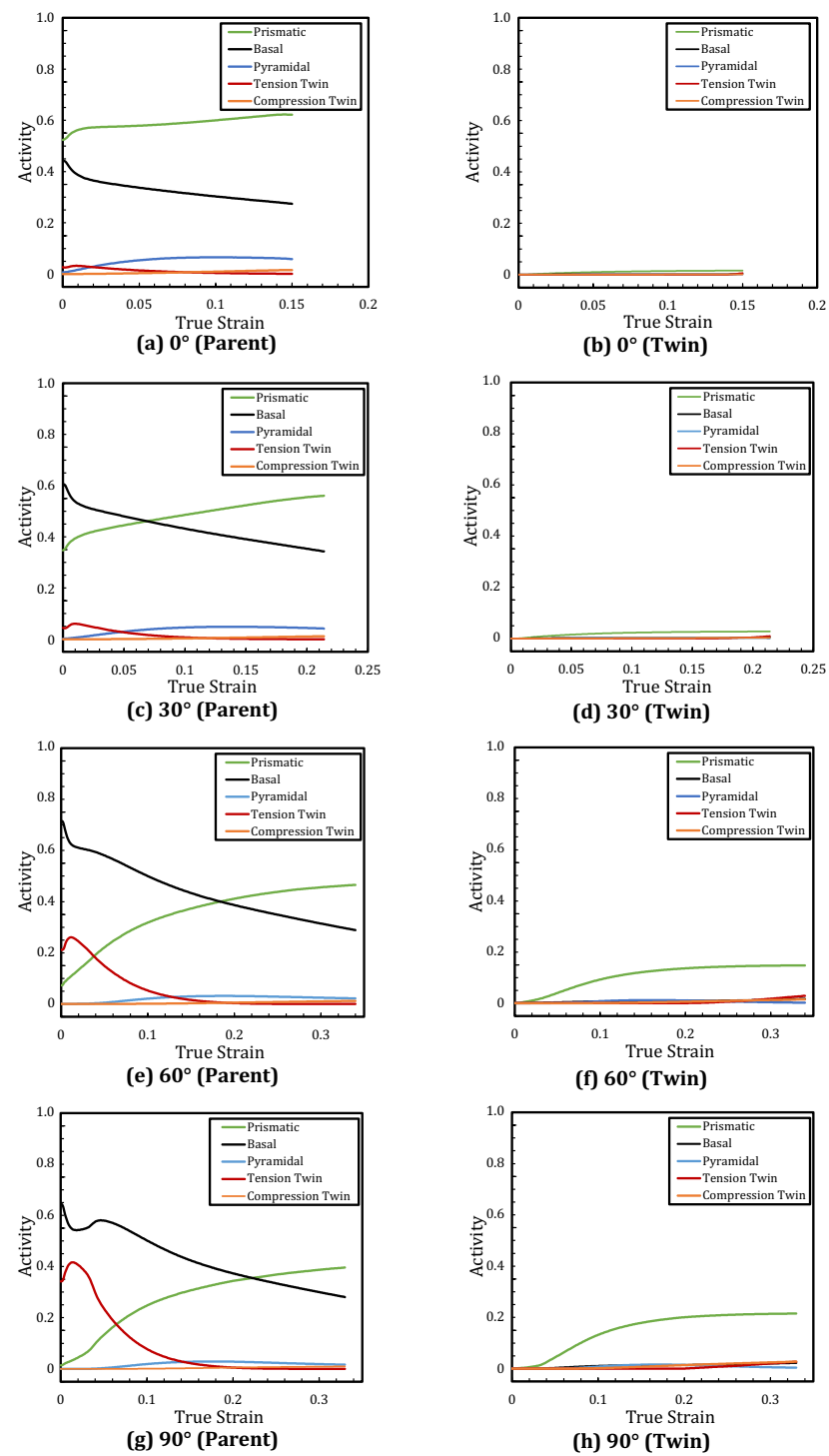
Figure 16. Activity of slip and twin within the parent (**a**,**c**,**e**,**g**) and primary twin (**b**,**d**,**f**,**g**) obtained from the simulations of ZEK100 at room temperature (293 K) and 0.001 s^{-1} strain-rate. Subplots (**a**–**d**) show compression activity and (**e**–**h**) show tension activity. Each row represents activity for 0°, 30°, 60°, and 90°, respectively.
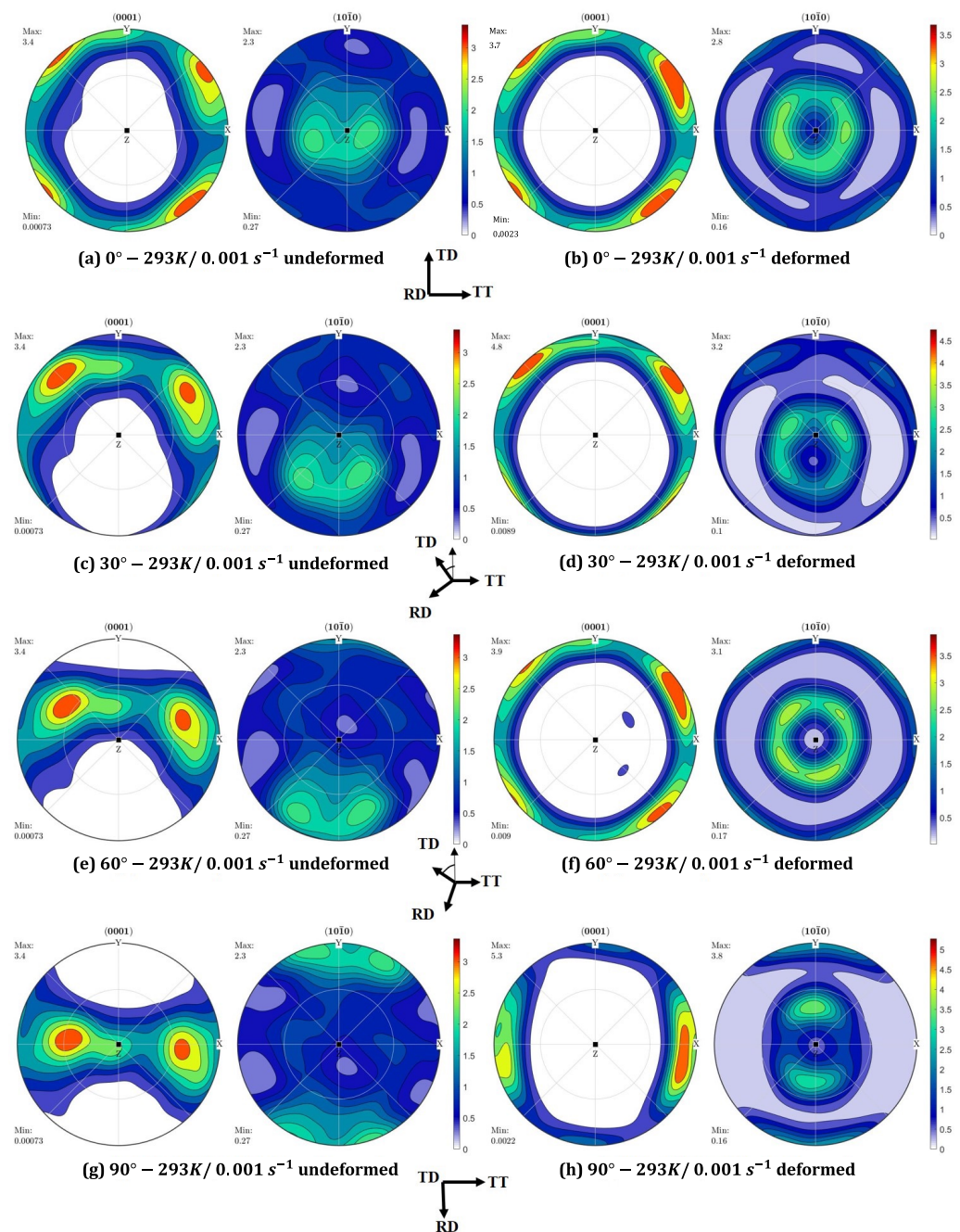
Figure 17. Pole figures in {0001} and {10$\bar{1}$0} representing texture evolution for ZEK100 at room temperature and 0.001 s^{-1} strain rate in tension. Plots (**a,c,e,g**) are undeformed texture and (**b,d,f,h**) are deformed texture from simulations strained in 0°, 30°, 60° and 90°, respectively.

3.4. Effect of Transmutation Scheme and Limitations

Over both alloys, the model prersented herein that incorporates transmutation scheme into temperature and strain rate independent composite grain VPSC model has captured the anisotropy and asymmetry of a strong textured and a weak textured magnesium alloy in the absence of Hall-Petch effects. The current model is also more reliable as it provides a physical basis to model the hardening observed in Regime II attributed to profuse twinning as an alternate to the Hall-Petch effect which in recent studies has proven to differ from experimental evidence and is inconsistent in predicting hardening behavior [22]. While most VPSC simulation efforts are made to predict limited scenarios in strain rate, temperature, and/or stress-states [23–25,36], the current model uses physics-

vetted mechanism of dislocation transmutation to predict deformation response with one set of parameters per alloy for all these varying conditions. However, the limitation of the current model includes over-prediction of the stress–strain behavior at higher temperatures, which can be a contribution from dynamic recrystallization (DRX) observed in magnesium at high temperatures. In their study of DRX in magnesium at high temperature deformation, Al-Samman et al. found that even at a relatively low temperature of 473 K and high strain rate, the center of the deformed sample went through DRX which caused softening [60]. The difference in the deformation behavior of the center and the lateral surface is attributed to the nonuniform distribution of strain in the sample seen commonly in uniaxial compression. Ulacia et al. [57] provide experimental evidence of microstructure fully recrystallizing at a low strain rate of 10^{-3} s^{-1} and 473 K temperature. The disagreement in fitting the model to the experimental curve can be observed for compression ND and RD at 473 K and 0.001 s^{-1} in Figure 11e,f. The incorporation of dynamic recrystallization is beyond the scope of the current work and will be a subject for future model enhancements.

4. Conclusions

The present work aims to better capture the anisotropy and asymmetry exhibited by HCP materials through the examination of magnesium alloys. To this end, a dislocation transmutation scheme is incorporated into a VPSC modeling framework to to capture the effects of twinning and slip dislocations on hardening. The goal of the model is to serve as a platform for the generation of more robust material models and subroutines to be used in the continuum-level simulation of HCP materials subject to varying starting crystallographic textures, stress-states, strain rates, temperatures, and load orientations. The updated model is validated using experiments performed on strongly textured (AZ31) and weakly textured (ZEK100) material, leading to the following major takeaways:

1. Monotonic testing at different strain rates, temperatures, loading directions, and stress-states performed on a rolled rolled AZ31 Mg alloy showed a strong strain rate sensitivity.
2. This strain rate sensitivity affected both the anisotropic and asymmetry behaviors of the alloys and have been poorly captured by past crystal plasticity models.
3. Improved ability to predict this behavior is achieved through the introduction of a physics-vetted mechanism, the dislocation transmutation effect, providing the proper additional mathematical latitude for fitting stress–strain responses and textures.
4. Monotonic testing of weakly textured ZEK100 at varying temperatures and loading directions revealed substantial in-plane anisotropy.
5. Previous studies lacked the right mechanism to give us the mathematical flexibility to adequately capture this anisotropy. The proposed model fares well at this task and validates the transmutation mechanism by capturing the overall variation using a singular set of material modeling parameter values across all test cases.

Author Contributions: Conceptualization, M.P. and H.E.K.; investigation, M.P., Y.P. and H.E.K.; methodology, M.P., Y.P. and H.E.K.; resources, H.R. and H.E.K.; supervision, H.R. and H.E.K.; validation, M.P., Y.P. and S.M.; visualization, M.P., Y.P. and S.M.; writing—original draft, M.P.; writing—review and editing, Y.P. and S.M. All authors have read and agreed to the published version of the manuscript.

Data Availability Statement: Data generated and supporting the findings of this article are available from the corresponding author upon reasonable request.

Conflicts of Interest: The authors declare no conflict of interest regarding the design, experimentation, simulation, or analysis aspects of the work presented in this manuscript.

References

1. Takuda, H.; Yoshii, T.; Hatta, N. Finite-Element Analysis of the Formability of a Magnesium-Based Alloy AZ31 Sheet. *J. Mater. Process. Technol.* **1999**, *89–90*, 135–140. [CrossRef]
2. Mordike, B.L.; Ebert, T. Magnesium: Properties—Applications—Potential. *Mater. Sci. Eng. A* **2001**, *302*, 37–45. [CrossRef]
3. Kelley, E.; Hosford, W. Plane-strain compression of magnesium and magnesium alloy crystals. *Trans. Met. Soc. AIME* **1968**, *242*, 5–13.
4. Jain, A.; Agnew, S.R. Modeling the Temperature Dependent Effect of Twinning on the Behavior of Magnesium Alloy AZ31B Sheet. *Mater. Sci. Eng. A* **2007**, *462*, 29–36. [CrossRef]
5. Taylor, G.I. Plastic strain in metals. *Our. Inst. Metals.* **1938**, *62*, 307–324.
6. Agnew, S.R.; Duygulu, Ö. Plastic Anisotropy and the Role of Non-Basal Slip in Magnesium Alloy AZ31B. *Int. J. Plast.* **2005**, *21*, 1161–1193. [CrossRef]
7. Yoo, M.H. Slip, Twinning, and Fracture in Hexagonal Close-Packed Metals. *Metall. Trans. A* **1981**, *12*, 409–418. [CrossRef]
8. Russell, W.D.; Bratton, N.R.; Paudel, Y.; Moser, R.D.; McClelland, Z.B.; Barrett, C.D.; Oppedal, A.L.; Whittington, W.R.; Rhee, H.; Mujahid, S.; et al. In Situ Characterization of the Effect of Twin-Microstructure Interactions on {1 0 1 2} Tension and {1 0 1 1} Contraction Twin Nucleation, Growth and Damage in Magnesium. *Metals* **2020**, *10*, 1403. [CrossRef]
9. Paudel, Y.; Giri, D.; Priddy, M.W.; Barrett, C.D.; Inal, K.; Tschopp, M.A.; Rhee, H.; El Kadiri, H. A review on capturing twin nucleation in crystal plasticity for hexagonal metals. *Metals* **2021**, *11*, 1373. [CrossRef]
10. Paudel, Y.; Barrett, C.; Mujahid, S.; Rhee, H.; El Kadiri, H. Micromechanics-based strain energy study of {1 0 $\bar{1}$ 2} twin-band pattern in a three-point bend Mg alloy. *J. Mater. Res.* **2022**, *38*, 461–472. [CrossRef]
11. Reed-Hill, R.E.; Robertson, W.D. Additional Modes of Deformation Twinning in Magnesium. *Acta Metall.* **1957**, *5*, 717–727. [CrossRef]
12. Koike, J.; Sato, Y.; Ando, D. Origin of the Anomalous 10\bar12 Twinning during Tensile Deformation of Mg Alloy Sheet. *Mater. Trans.* **2008**, *49*, 2792–2800. [CrossRef]
13. Oppedal, A.L.; El Kadiri, H.; Tomé, C.N.; Kaschner, G.C.; Vogel, S.C.; Baird, J.C.; Horstemeyer, M.F. Effect of Dislocation Transmutation on Modeling Hardening Mechanisms by Twinning in Magnesium. *Int. J. Plast.* **2012**, *30–31*, 41–61. [CrossRef]
14. Tomé, C.N.; Maudlin, P.J.; Lebensohn, R.A.; Kaschner, G.C. Mechanical Response of Zirconium—I. Derivation of a Polycrystal Constitutive Law and Finite Element Analysis. *Acta Mater.* **2001**, *49*, 3085–3096. [CrossRef]
15. El Kadiri, H.; Barrett, C.D.; Tschopp, M.A. The Candidacy of Shuffle and Shear during Compound Twinning in Hexagonal Close-Packed Structures. *Acta Mater.* **2013**, *61*, 7646–7659. [CrossRef]
16. Tomé, C.N.; Lebensohn, R.A.; Kocks, U.F. A Model for Texture Development Dominated by Deformation Twinning: Application to Zirconium Alloys. *Acta Metall. Mater.* **1991**, *39*, 2667–2680. [CrossRef]
17. Lebensohn, R.A.; Tomé, C.N. A Self-Consistent Anisotropic Approach for the Simulation of Plastic Deformation and Texture Development of Polycrystals: Application to Zirconium Alloys. *Acta Metall. Mater.* **1993**, *41*, 2611–2624. [CrossRef]
18. Kalidindi, S.R. Incorporation of Deformation Twinning in Crystal Plasticity Models. *J. Mech. Phys. Solids* **1998**, *46*, 267–290. [CrossRef]
19. Proust, G.; Tomé, C.N.; Kaschner, G.C. Modeling Texture, Twinning and Hardening Evolution during Deformation of Hexagonal Materials. *Acta Mater.* **2007**, *55*, 2137–2148. [CrossRef]
20. Paudel, Y.; Barrett, C.D.; El Kadiri, H. Full-Field Crystal Plasticity Modeling of {1 0 $\bar{1}$ 2} Twin Nucleation. In *Magnesium Technology 2020*; Jordon, J.B., Miller, V., Joshi, V.V., Neelameggham, N.R., Eds.; The Minerals, Metals & Materials Series; Springer: Berlin/Heidelberg, Germany, 2020; pp. 141–146. [CrossRef]
21. Long, X.; Chong, K.; Su, Y.; Du, L.; Zhang, G. Connecting the macroscopic and mesoscopic properties of sintered silver nanoparticles by crystal plasticity finite element method. *Eng. Fract. Mech.* **2023**, *281*, 109137. [CrossRef]
22. El Kadiri, H.; Oppedal, A.L. A Crystal Plasticity Theory for Latent Hardening by Glide Twinning through Dislocation Transmutation and Twin Accommodation Effects. *J. Mech. Phys. Solids* **2010**, *58*, 613–624. [CrossRef]
23. Tam, K.J.; Vaughan, M.W.; Shen, L.; Knezevic, M.; Karaman, I.; Proust, G. Modelling the temperature and texture effects on the deformation mechanisms of magnesium alloy AZ31. *Int. J. Mech. Sci.* **2020**, *182*, 105727. [CrossRef]
24. Chen, Q.; Hu, L.; Shi, L.; Zhou, T.; Yang, M.; Tu, J. Assessment in predictability of visco-plastic self-consistent model with a minimum parameter approach: Numerical investigation of plastic deformation behavior of AZ31 magnesium alloy for various loading conditions. *Mater. Sci. Eng. A* **2020**, *774*, 138912. [CrossRef]
25. Kabirian, F.; Khan, A.S.; Gnäupel-Herold, T. Visco-plastic modeling of mechanical responses and texture evolution in extruded AZ31 magnesium alloy for various loading conditions. *Int. J. Plast.* **2015**, *68*, 1–20. [CrossRef]
26. Xie, Y.; Li, S. Geometrically-Compatible Dislocation Pattern and Modeling of Crystal Plasticity in Body-Centered Cubic (BCC) Crystal at Micron Scale. *CMES-Comput. Model. Eng. Sci.* **2021**, *129*, 1419–1440. [CrossRef]
27. Molinari, A.; Canova, G.R.; Ahzi, S. A Self Consistent Approach of the Large Deformation Polycrystal Viscoplasticity. *Acta Metall.* **1987**, *35*, 2983–2994. [CrossRef]
28. Karaman, I.; Sehitoglu, H.; Beaudoin, A.J.; Chumlyakov, Y.I.; Maier, H.J.; Tomé, C.N. Modeling the Deformation Behavior of Hadfield Steel Single and Polycrystals Due to Twinning and Slip. *Acta Mater.* **2000**, *48*, 2031–2047. [CrossRef]

29. Kok, S.; Beaudoin, A.J.; Tortorelli, D.A. On the Development of Stage IV Hardening Using a Model Based on the Mechanical Threshold. *Acta Mater.* **2002**, *50*, 1653–1667. [CrossRef]

30. Beyerlein, I.J.; Tomé, C.N. A Dislocation-Based Constitutive Law for Pure Zr Including Temperature Effects. *Int. J. Plast.* **2008**, *24*, 867–895. [CrossRef]

31. Lavrentev, F.F. The Type of Dislocation Interaction as the Factor Determining Work Hardening. *Mater. Sci. Eng.* **1980**, *46*, 191–208. [CrossRef]

32. Essmann, U.; Mughrabi, H. Annihilation of Dislocations during Tensile and Cyclic Deformation and Limits of Dislocation Densities. *Philos. Mag. A* **1979**, *40*, 731–756. [CrossRef]

33. Mecking, H.; Kocks, U.F. Kinetics of Flow and Strain-Hardening. *Acta Metall.* **1981**, *29*, 1865–1875. [CrossRef]

34. Dorn, J.E.; Mitchell, J.B. *Slip Mechanisms in Single Crystals of Hexagonal Close-Packed Phases*; University of California: Los Angeles, CA, USA, 1964.

35. Basinski, Z.S.; Szczerba, M.S.; Niewczas, M.; Embury, J.D.; Basinski, S.J. The Transformation of Slip Dislocations during Twinning of Copper-Aluminum Alloy Crystals. *Rev. Métallurgie* **1997**, *94*, 1037–1044. [CrossRef]

36. Allen, R.M.; Toth, L.S.; Oppedal, A.L.; El Kadiri, H. Crystal Plasticity Modeling of Anisotropic Hardening and Texture Due to Dislocation Transmutation in Twinning. *Materials* **2018**, *11*, 1855. [CrossRef] [PubMed]

37. Paudel, Y.; Indeck, J.; Hazeli, K.; Priddy, M.W.; Inal, K.; Rhee, H.; Barrett, C.D.; Whittington, W.R.; Limmer, K.R.; El Kadiri, H. Characterization and modeling of {101 2} twin banding in magnesium. *Acta Mater.* **2020**, *183*, 438–451. [CrossRef]

38. Tan, C.W.; Xu, S.N.; Wang, L.; Chen, Z.Y.; Wang, F.C.; Cai, H.N. Effect of Temperature on Mechanical Behavior of AZ31 Magnesium Alloy. *Trans. Nonferrous Met. Soc. China* **2007**, *17*, 41–45. [CrossRef]

39. Kurukuri, S.; Worswick, M.J.; Ghaffari Tari, D.; Mishra, R.K.; Carter, J.T. Rate Sensitivity and Tension–Compression Asymmetry in AZ31B Magnesium Alloy Sheet. *Philos. Trans. R. Soc. A Math. Phys. Eng. Sci.* **2014**, *372*, 20130216. [CrossRef]

40. Agnew, S.R.; Duygulu, O. A Mechanistic Understanding of the Formability of Magnesium: Examining the Role of Temperature on the Deformation Mechanisms. *Mater. Sci. Forum* **2003**, *419–422*, 177–188. [CrossRef]

41. Agnew, S.R.; Yoo, M.H.; Tomé, C.N. Application of Texture Simulation to Understanding Mechanical Behavior of Mg and Solid Solution Alloys Containing Li or Y. *Acta Mater.* **2001**, *49*, 4277–4289. [CrossRef]

42. Meyers, M.A.; Armstrong, R.W.; Kirchner, H.O.K. *Mechanics and Materials: Fundamentals and Linkages*; Wiley: Hoboken, NJ, USA, 1999.

43. Kannan, V.; Hazeli, K.; Ramesh, K. The mechanics of dynamic twinning in single crystal magnesium. *J. Mech. Phys. Solids* **2018**, *120*, 154–178. [CrossRef]

44. Kurukuri, S.; Worswick, M.J.; Bardelcik, A.; Mishra, R.K.; Carter, J.T. Constitutive Behavior of Commercial Grade ZEK100 Magnesium Alloy Sheet over a Wide Range of Strain Rates. *Metall. Mater. Trans. A* **2014**, *45*, 3321–3337. [CrossRef]

45. Al-Samman, T.; Li, X. Sheet Texture Modification in Magnesium-Based Alloys by Selective Rare Earth Alloying. *Mater. Sci. Eng. A* **2011**, *528*, 3809–3822. [CrossRef]

46. Bohlen, J.; Nürnberg, M.R.; Senn, J.W.; Letzig, D.; Agnew, S.R. The Texture and Anisotropy of Magnesium–Zinc–Rare Earth Alloy Sheets. *Acta Mater.* **2007**, *55*, 2101–2112. [CrossRef]

47. Mackenzie, L.W.F.; Pekguleryuz, M.O. The Recrystallization and Texture of Magnesium–Zinc–Cerium Alloys. *Scr. Mater.* **2008**, *59*, 665–668. [CrossRef]

48. Aslam, I.; Li, B.; McClelland, Z.; Horstemeyer, S.J.; Ma, Q.; Wang, P.T.; Horstemeyer, M.F. Three-Point Bending Behavior of a ZEK100 Mg Alloy at Room Temperature. *Mater. Sci. Eng. A* **2014**, *590*, 168–173. [CrossRef]

49. Khan, A.S.; Pandey, A.; Gnäupel-Herold, T.; Mishra, R.K. Mechanical Response and Texture Evolution of AZ31 Alloy at Large Strains for Different Strain Rates and Temperatures. *Int. J. Plast.* **2011**, *27*, 688–706. [CrossRef]

50. Niewczas, M. Lattice Correspondence during Twinning in Hexagonal Close-Packed Crystals. *Acta Mater.* **2010**, *58*, 5848–5857. [CrossRef]

51. El Kadiri, H.; Barrett, C.D.; Wang, J.; Tomé, C.N. Why Are {10$\bar{1}$ 2} Twins Profuse in Magnesium? *Acta Mater.* **2015**, *85*, 354–361. [CrossRef]

52. *MATLAB*, version 9.13.0 (R2020b); The MathWorks Inc.: Natick, MA, USA, 2020.

53. Wang, Z.Q.; Chapuis, A.; Liu, Q. Simulation of Mechanical Behavior of AZ31 Magnesium Alloy during Twin-Dominated Large Plastic Deformation. *Trans. Nonferrous Met. Soc. China* **2015**, *25*, 3595–3603. [CrossRef]

54. Ardeljan, M.; Beyerlein, I.J.; McWilliams, B.A.; Knezevic, M. Strain Rate and Temperature Sensitive Multi-Level Crystal Plasticity Model for Large Plastic Deformation Behavior: Application to AZ31 Magnesium Alloy. *Int. J. Plast.* **2016**, *83*, 90–109. [CrossRef]

55. Oppedal, A.; El Kadiri, H.; Tomé, C.; Vogel, S.C.; Horstemeyer, M. Anisotropy in Hexagonal Close-Packed Structures: Improvements to Crystal Plasticity Approaches Applied to Magnesium Alloy. *Philos. Mag.* **2013**, *93*, 4311–4330. [CrossRef]

56. Jiang, L.; Jonas, J.J.; Mishra, R.K.; Luo, A.A.; Sachdev, A.K.; Godet, S. Twinning and Texture Development in Two Mg Alloys Subjected to Loading along Three Different Strain Paths. *Acta Mater.* **2007**, *55*, 3899–3910. [CrossRef]

57. Ulacia, I.; Dudamell, N.V.; Gálvez, F.; Yi, S.; Pérez-Prado, M.T.; Hurtado, I. Mechanical Behavior and Microstructural Evolution of a Mg AZ31 Sheet at Dynamic Strain Rates. *Acta Mater.* **2010**, *58*, 2988–2998. [CrossRef]

58. Griffiths, D.; Davis, B.; Robson, J.D. The Influence of Strain Path on Rare Earth Recrystallization Textures in a Magnesium-Zinc-Rare Earth Alloy. *Metall. Mater. Trans. A* **2018**, *49*, 321–332. [CrossRef]

59. Ge, H. Development of a Genetic Algorithm Approach to Calibrate the EVPSC Model. Ph.D. Thesis, McMaster University, Hamilton, ON, Canada, 2016.

60. Al-Samman, T.; Gottstein, G. Dynamic Recrystallization during High Temperature Deformation of Magnesium. *Mater. Sci. Eng. A* **2008**, *490*, 411–420. [CrossRef]